FORCE SPECTROSCOPY USING BIMODAL ATOMIC FORCE MICROSCOPY

A THESIS

SUBMITTED TO THE DEPARTMENT OF ELECTRICAL AND

ELECTRONICS ENGINEERING

AND THE INSTITUTE OF ENGINEERING AND SCIENCES

OF BILKENT UNIVERSITY

IN PARTIAL FULFILLMENT OF THE REQUIREMENTS

FOR THE DEGREE OF

MASTER OF SCIENCE

By

Mehmet Deniz Aksoy

August 2010

I certify that I have read this thesis and that in my opinion it is fully adequate, in scope and in quality, as a thesis for the degree of Master of Science.

Prof. Dr. Abdullah Atalar(Supervisor)

I certify that I have read this thesis and that in my opinion it is fully adequate, in scope and in quality, as a thesis for the degree of Master of Science.

Prof. Dr. Hayrettin Köymen

I certify that I have read this thesis and that in my opinion it is fully adequate, in scope and in quality, as a thesis for the degree of Master of Science.

Assistant Prof. Coşkun Kocabaş

Approved for the Institute of Engineering and Sciences:

Prof. Dr. Levent Onural
Director of Institute of Engineering and Sciences

ABSTRACT

FORCE SPECTROSCOPY USING BIMODAL ATOMIC FORCE MICROSCOPY

Mehmet Deniz Aksoy
M.S. in Electrical and Electronics Engineering
Supervisor: Prof. Dr. Abdullah Atalar
August 2010

In atomic force microscopy (AFM) achieving compositional contrast while mapping topographical features is a challenging task. Conventional single mode frequency and amplitude modulation AFM techniques are sensitive to the properties of the tip sample interaction, however in the absence of additional information channels, compositional features such as elasticity and density cannot be distinguished from topographical variations. To tackle this problem bimodal excitation techniques are introduced. In bimodal amplitude modulation AFM, sensitivity to compositional features improves by recording the phase of the higher order vibrations, while the topography is acquired using the amplitude of the first order vibrations. Increased sensitivity to mechanical properties allows imaging delicate samples such as organic molecules using gentle forces.

In this thesis we propose a force spectroscopy technique in which two modes of a cantilever are excited in such a way that the amplitudes of the components of the vibration stay constant. Presence of the force field modulates the properties

of the primarily bi-harmonic vibration of the cantilever, which is, in our case, the instantaneous frequencies of vibration modes. The frequency shift of the first mode remains sensitive to topographical variation, whereas the frequency shift of the higher mode samples the gradient of the tip sample forces and allows us to extract the tip sample interaction as a function of separation within a single cycle of the slow oscillation.

We provide an analytic treatment of the proposed scheme and confirm our predictions by numerical simulations. We present an analysis of the sensitivity of higher mode frequency shifts to compositional features in the presence of thermal and sensor noise. We demonstrate that the method is suitable for the fast acquisition of contact properties, especially in vacuum environment where the large quality factor of the cantilever limits the available bandwidth of the amplitude modulation techniques. Finally we investigate phase shifts in bimodal amplitude modulation AFM using the developed formalism and show that phase contrast can be optimized by solving a simpler problem in single mode amplitude modulation AFM.

Keywords: Atomic Force Microscopy, Dynamic Atomic Force Microscopy, Bimodal Imaging, Bimodal Excitation, Frequency Modulation Atomic Force Microscopy, Amplitude Modulation Atomic Force Microscopy, Force Spectroscopy

ÖZET

ÇİFT MODLU ATOMİK KUVVET MİKROSKOBU TEKNİĞİ KULLANARAK KUVVET SPEKTROSKOPİSİ

Mehmet Deniz Aksoy
Elektrik ve Elektronik Mühendisligi Bölümü Yüksek Lisans
Tez Yöneticisi: Prof. Dr. Abdullah Atalar
Ağustos 2010

Atomik kuvvet mikroskobu (AKM) kullanarak bir yüzeyin topoğrafya ve bileşen analizlerinin aynı anda yapılması başlı başına zor bir problemdir. Frekans ve genlik kiplemesi kullanan standart AKM teknikleri yüzey kuvvetlerinin özelliklerine duyarlı olsa da, ek bilgi kanallarının yokluğu durumunda yüzey bileşen bilgisi ile topoğrafya bilgisi kolaylıkla karıştırılmaktadır. Yakın geçmişte bu problemi çözmek amacıyla kuvvet sensörünün birden çok modunun titreştirildiği teknikler kullanılmaya başlanmıştır. Genlik kiplemesi kullanılan, kuvvet sensörünün iki modunun titreştirildiği AKM tekniğininde ikinci modun fazı kullanılarak yüzeyin kimyasal özelliklerine olan duyarlılığı arttırmak, aynı zamanda ilk modun genliği kullanılarak yüzeyin haritasını çıkartmak mümkündür. Artan duyarlılık sayesinde hassas örnekler küçük kuvvetler kullanılarak incelenebilmektedir.

Bu tezde hızlı bir kuvvet spektroskopisi tekniği önermekteyiz. Kuvvet sensörünün iki modu genlikleri sabit kalacak şekilde titreştirilir. Yüzey kuvvetlerinin varlığı bu ikili titreşimin özelliklerini değiştirir. Genlikler sabit tutulduğu için titreşimin anlık frekansları değişir. Birinci modun frekans değişimleri topoğrafik özelliklere duyarlı kalırken, rezonans frekansı yüksek olan modun anlık frekansı yüzey kuvvetlerinin türevi ile doğru orantılı olarak değişir. Böylece yüzeyin yükselik haritasını çıkarmaktan öte, her noktanın üzerindeki kuvvetleri öğrenmek, dolayısıyla incelenen yüzeyin kimyasal özelliklerini de hızla haritalamak mümkün olabilir.

Önerilen tekniğin matematiksel özelliklerini araştırdıktan sonra sonuçlarımızı sayısal simülasyonlarla destekleyeceğiz. Bunun yanı sıra frekans kaymalarının yüzey özelliklerine duyarlılığını termal ve sensör gürültüsünün varlığında inceleyeceğiz. Son olarak genlik kiplemesi kullanılan çift modlu AKM tekniğindeki faz kontrast mekanizmasını anlamaya çalışacağız.

Anahtar Kelimeler: Atomik Kuvvet Mikroskobu, Çift Modlu Görüntüleme, Çift Modlu Titreştirme, Çift Modlu Frekans Kipleme Tekniği, Kuvvet Spektroskopisi

ACKNOWLEDGMENTS

I owe my most sincere gratitude to my supervisor Professor Abdullah Atalar, a legend and by all account a great man, for his invaluable guidance throughout my graduate studies. His understanding and patience was of great value for me. I warmly thank to Professor Ergin Atalar for his endless support and kindness with me. He was the only one I could talk to when I was in despair. I am grateful to all my Professors, especially Orhan Arikan, from my undergraduate studies in Bilkent University. During the course of the writing of this thesis I have seen how much I have learnt from them.

Thanks to my research partners Burak Selvi and Vahdettin Tas for fruitful discussions. They were generous. I am indepted to my former and current officemates Ustun Ozgur, Can Bal, Ceyhun Kelleci, Selim Olcum, Niyazi Senlik and Elif Aydogdu for making things better for me. I wish to thank Cemal Albayrak, Yigit Subasi, Can Afacan, Erdem Ozcan, Bugra Akcan, Emre Sari, Can Uran; wonderful friends I have made during my 8 years in Bilkent University. Their companionship was valuable more than anything.

Finally I thank to my parents Ozer and Emel, my little brother Onur and my sweet darling Ayse for always believing in me no matter what. None of this would have been possible without them.

Contents

List of Figures

Dedicated to friends

Chapter 1

INTRODUCTION

Since its invention atomic force microscopy (AFM) is used in vast variety of applications and has proven to be a powerful tool in nanometer science [1]. Although nano-scale and even atomic-scale resolution of the surface topography achieved by AFM reveals a lot of information about the sample, it is also desirable to identify and differentiate compositional features such as its elasticity and density.

It is possible to perform frequency-versus-distance measurements by tracking frequency changes of a vibrating lever to calculate tip-sample forces [2, 3]. Such spectroscopic measurements suffer from lateral and vertical thermal drift and and imaging speed is severely reduced by the requirement of scanning in the normal direction [4].

Several techniques are proposed for simultaneous and faster acquisition of the contact properties and the topographical information. Sahin *et al.* introduced the use of harmonic cantilevers to recover time resolved forces acting on the tip from harmonics generated by the nonlinear tip-sample interaction [5, 6]. Recently, bimodal amplitude modulation AFM technique is developed where a high order

flexural mode is excited simultaneously with the first to achieve increased phase sensitivity to compositional features at the higher order mode [7, 8, 9].

In this thesis, we propose a force spectroscopy technique where a higher order mode of a cantilever is excited simultaneously with the first. Resonance tracking of both vibration modes through frequency modulation scheme provides a way to extract topographical information and the gradient of the tip-sample interaction within a single surface scan.

In Chapter 2, we provide mathematical preliminaries that are necessary for the development of the thesis work, review tip sample forces and fundamental operating modes of atomic force microscopy, draw minor conclusions, and state challenges faced by force microscopy community. In Chapter 3 we review existing techniques for the simultaneous acquisition of contact properties and the topographical information, namely bimodal amplitude modulation AFM and the harmonic imaging.

In Chapter 4, we provide an analytic treatment of the proposed scheme, derive expressions relating observables of the system and the tip sample interaction, and offer algorithms for the recovery and the quantification of surface forces. We confirm our predictions by numerical simulations, and present an analysis on the force sensitivity of the higher mode frequency shifts in the presence of thermal and sensor noise. In Chapter 5 we investigate phase shifts in bimodal amplitude modulation AFM using the developed formalism and demonstrate that phase contrast can be optimized by solving a simpler problem in single mode amplitude modulation AFM. We conclude and list future research directions in the Chapter 6.

Chapter 2

PRINCIPLES OF ATOMIC FORCE MICROSCOPY

2.1 Overview

A complete understanding of AFM operation requires us to solve the equation of motion of a cantilevered beam under the effect of the tip sample forces. Governing equation of motion is the Euler-Bernoulli beam equation [10]:

$$\frac{EI}{L^4}\frac{\partial^4}{\partial x^4}\left(z(x,t)+\beta\frac{\partial z(x,t)}{\partial t}\right)+bh\rho_c\frac{\partial^2 z(x,t)}{\partial t^2}+\gamma\frac{\partial z(w,t)}{\partial t}=F(x,t) \qquad (2.1)$$

where E is the Young's modulus of the cantilever, I is the area moment of inertia, γ is the hydrodynamic damping coefficient, β is the internal damping coefficient, ρ is the mass density, b, h, and L are the width, height, and length of the rectangular cantilever respectively, $z(x,t)$ is the vertical displacement of the cantilever placed along the $\vec{x}$ axis, $F(x,t)$ is the force acting along the cantilever.

A time independent and homogenous solution of the aforementioned partial differential equation, subject to the constraint that one end of the beam is

clamped to a substrate, yields a set of mode shapes. They are called the *eigenmodes* of the cantilever and a unique resonance frequency corresponds to each of these eigenmodes. A mode shape can be excited by applying a time periodic force to the cantilever at the eigenmode's resonance frequency. Depending on the environmental conditions within which the cantilever is suspended there exists a quality factor Q_i and the stiffness or the spring constant k_i for each eigenmode with resonance centered at f_i. Throughout the thesis we are going to enumerate the eigenmodes starting from $i = 1$, unless otherwise is stated. Further, f_i and Q_i are going to represent the natural resonance frequency and the quality factor of the ith mode, respectively.

An eigenmode with a high quality factor means that the mode has less coupling with dissipative mechanisms such as hydrodynamic damping, thermoelastic dissipation, clamping losses and internal damping [11]. All dissipative mechanisms act in parallel and quality factor eventually determines mechanical mode's coupling to the heat bath therefore determines the thermal noise density, while thermal noise density roughly determines the maximum force sensitivity of the mechanical sensor. A high stiffness means less motional sensitivity to external excitations as stated by the Hooke's law $F = kz$. An eigenmode with low stiffness (therefore with high motional sensitivity) typically implies a smaller quality factor, therefore there exists a design tradeoff in choosing a mode's stiffness and its quality factor.

Usually, the motion of the tip of a cantilever itself is of interest. This motion can be described by a set of second order nonlinear differential equations to a good approximation [12]:

$$m_i \frac{d^2 z_i}{dt^2} + \frac{m_i \omega_i}{Q_i} \frac{dz_i}{dt} + k_i z_i = F_{ext}(t) = F_{ts}(d) + F_0 \cos(\omega t) \tag{2.2}$$

where z_i is the vertical displacement of the tip, m_i is the effective mass of the ith mode given by the relation $m_i = k_i/\omega_i^2$ where $\omega_i = 2\pi f_i$, $F_{ext}(t)$ represents the

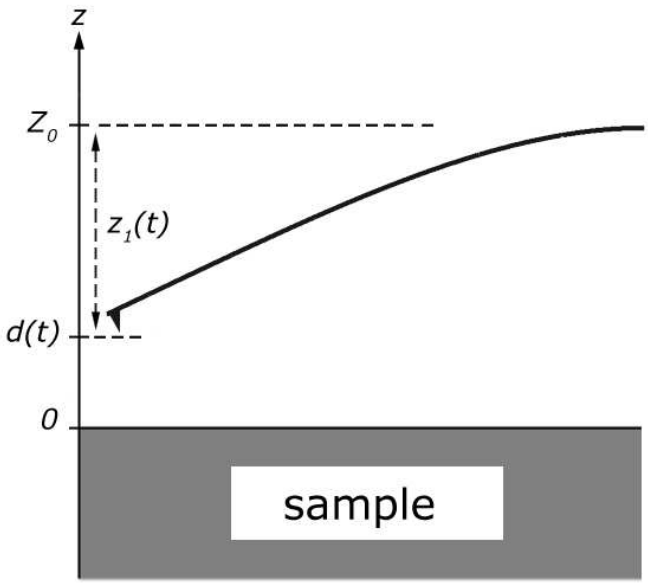

Figure 2.1: Schematic depiction of the flexural bending of a cantilevered beam and variables used to describe the tip position with respect to sample.

external forces acting on the tip which is the sum of tip sample forces $F_{ts}(d)$ and the drive $F_0 \cos(\omega t)$, $d = Z_0 + \sum_i z_i$ is the tip sample distance where Z_0 is the base sample separation. Fig. 2.1 shows some of these variables describing the motion of the tip along with the flexural bending of a cantilevered beam. Notice that in Eq. 2.2 modes are coupled through the nonlinear interaction described by the function $F_{ts}(d)$. Eventually, if experimental paramaters/inputs (k_i, Q_i, f_i, F_{ts}) are given, and the operating method or the relation between deliberate external drive and observables (i.e. relation between $F_0 \cos(\omega t)$ and z_i) is determined, a thorough understanding of the dynamics of AFM boils down to the comprehension of the system of nonlinear differential equations described by Eq. 2.2.

2.2 Tip-sample forces

Tip sample forces are fundamental to the understanding of AFM. Indeed, non-linear nature of the tip sample forces is the reason for the large number of mathematically intensive treatments on the subject, and for the occurrence of sophisticated, highly sensitive and at first glance counterintuitive microscopy techniques such as higher harmonic imaging and bimodal amplitude modulation AFM which were invented 15 years after AFM is first introduced in the late 80s.

The forces between the cantilever tip and the sample surface are not well-behaved as in sharply and monotonically decreasing tunnelling currents in scanning probe microscopy (SPM). The forces arise from the electromagnetic interactions between the molecules and atoms. These are van der Waals forces due to field fluctuations, short range chemical and ionic repulsive forces of atoms and molecules, adhesion and capillary forces [13]. The presence of van der Waals forces between the sample and the tip means that there is an attractive regime of interaction.

We are going to present a simple yet an adequate treatment of tip sample forces. Lennard-Jones potential is a simple mathematical model to describe the interaction between two atoms or molecules and is given by [14]:

$$U(r) = \frac{c_1}{r^{12}} - \frac{c_2}{r^6} \tag{2.3}$$

where r is the distance between two molecules, and c_1 and c_2 are interaction constants. Consider a single molecule of the sharp AFM tip positioned at r. Then, the interaction potential between that single molecule and the semi-infinite surface can be evaluated by a double integration of Eq. 2.3 to yield [15]:

$$U(r) = \frac{2\pi\rho_1 c_1}{90r^9} - \frac{2\pi\rho_1 c_2}{12r^3} \tag{2.4}$$

where ρ_1 is the mass density of the surface. The tip is not just a single molecule, instead, can be assumed as a sphere of radius R. See Fig. 2.2. Therefore,

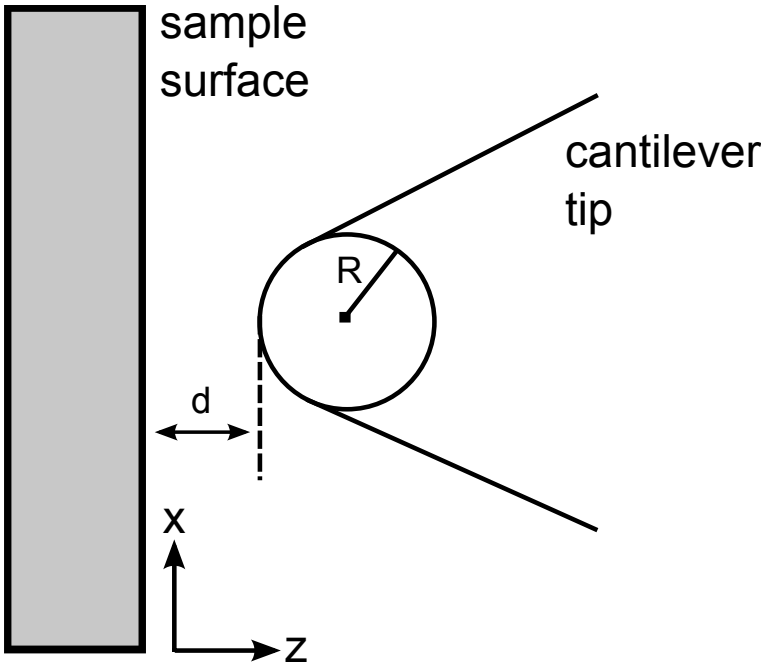

Figure 2.2: Schematic depiction of a cantilever tip with a radius R. Tip sample distance is d.

integrating the last expression over the volume of a spherical tip with the distance between its apex and the surface being d, we arrive at the interaction potential between the spherical tip and the semi-infinite surface:

$$U(d) = \frac{H_1 R}{1260 d^7} - \frac{H_2 R}{6d} \tag{2.5}$$

given that $R >> d$. $H_1 = \pi^2 \rho_1 \rho_2 c_1$ and $H_2 = \pi^2 \rho_1 \rho_2 c_2$ are the Hamaker constants for the repulsive and attractive potentials, respectively and ρ_2 is the mass density of the spherical tip. Consequently, the tip sample forces are given by minus the derivative of Eq. 2.5 with respect to tip sample separation d:

$$F_{Lennard}(d) = \frac{7 H_1 R}{1260 d^6} - \frac{H_2 R}{6 d^2} \tag{2.6}$$

Notice that the forces blow to very large values as the tip sample distance d becomes small.

Up to now we assumed that sample and tip are perfectly rigid. However, during contact, elastoplastic deformations occur [16]. Continuum elasticity theories describe the contact and adhesion of two bodies in the presence of external

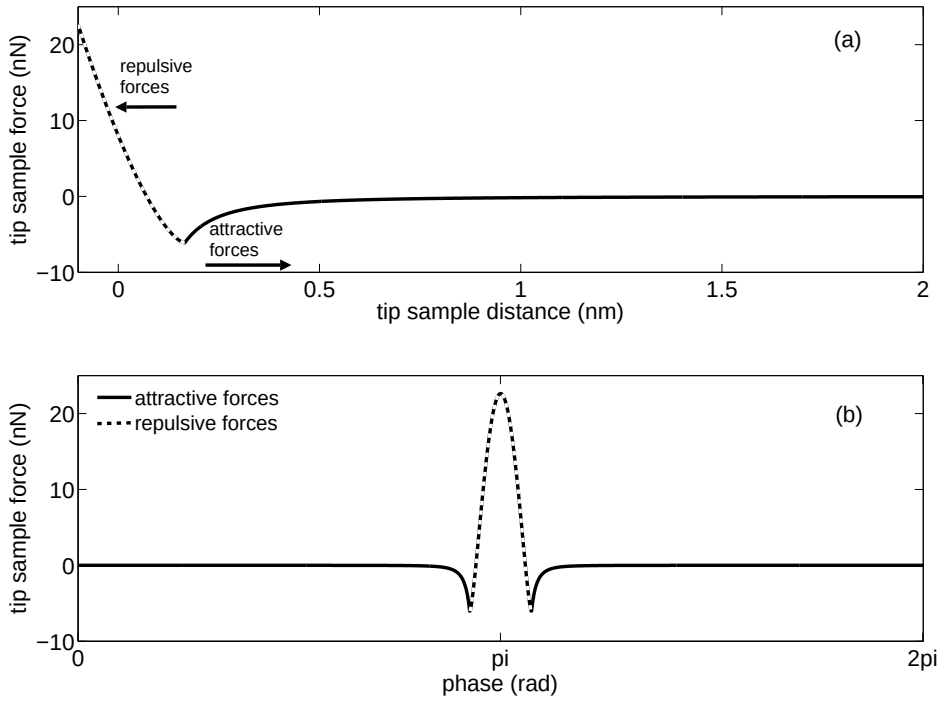

Figure 2.3: Tip sample forces according to DMT model. Forces are with respect to tip sample distance in (a) and with respect to time in (b). d(t) is assumed to be sinusoidal. Contact properties: $E = 50$ GPa, $H = 10 \cdot 10^{-20}$, $a_0 = 0.165$ nm, $R = 10$ nm.

forces [13]. While Hertz theory describes the problem without adhesion forces, Derjaguin-Muller-Toporov (DMT) theory is suitable for describing stiff contacts and small tip radii. In DMT theory, given that apex of the spherical tip is away from the surface by d, the contact force is given by [17]:

$$F_{DMT}(d) = \frac{4}{3} E \sqrt{R} (a_0 - d)^{\frac{3}{2}}, d \leq a_0 \tag{2.7}$$

where a_0 is the interatomic distance, below which repulsive forces start to dominate, and E is the Young's modulus which is the mechanical stiffness of a material while elongating or compressing. Young's modulus is the measure of stiffness of an elastic and isotropic body and is defined as the ratio of the uniaxial stress and strain. Young's modulus has the units of N m^{-2}.

We can assume that for $d > a_0$ the tip spends time only in the attractive regime, and for $d \leq a_0$ the tip experiences repulsive forces as described in the DMT theory. Then, the tip-sample forces can be written by combining Eqs. 2.6-2.7 and imposing continuity, therefore using a piecewise function:

$$F_{ts}(d) = \begin{cases} \frac{-HR}{6d^2} & d > a_0 \\ \frac{-HR}{6a_o^2} + \frac{4}{3}E\sqrt{R}(a_0 - d)^{\frac{3}{2}} & d \leq a_0 \end{cases} \tag{2.8}$$

where $H = H_2$ is the Hamaker constant of the sample. We call the piecewise model of the tip-sample force described in Eq. 2.8 as the DMT model. It is important to note that forces depend only on the tip-sample distance in DMT model once parameters of the tip and the sample (E, H, a_0, R) are fixed. Therefore, given a tip position with respect to sample $d(t)$, it is possible to calculate $F_{ts}(t)$ by plugging in $d(t)$ into 2.8. See Fig. 2.3 for a demonstration.

In DMT model, the forces between the tip and the sample are conservative. A conservative modelling of forces neglects the dissipation at the tip-sample contact (such as friction) and the losses are due to lever's intrinsic dissipation mechanisms such as clamping losses, internal damping and hydrodynamic damping which is the most dominant in ambient conditions. These loss mechanisms are modelled by the finite quality factor Q of the mode. The dissipation due to tip-sample forces can be described by modelling the motion of the sample by an additional degree of freedom of a damped oscillator and using a Lennard-Jones type tip sample interaction. Another way of doing this is to define velocity dependent forces and to incorporate them into the DMT model. In this thesis we are not concerned with the energy that is lost during tip-sample contact, therefore DMT model as in Eq. 2.8 or force definitions similar to DMT model are preferred.

2.3 Operating modes of AFM

A generic AFM setup consists of a micromechanical force sensor —typically a cantilevered beam—, a piezoelectric actuator which is used to excite the cantilever by time periodic forces, an XYZ piezo-scanner for raster and vertical scanning, an optical or piezoresistive detection setup used to convert mechanical deflections of the lever to the electrical domain, and feedback electronics to control the scan speed in the lateral direction and sample height in the vertical direction.

The probing tip, the cantilever, is brought into the close vicinity of the sample surface, whose mechanical properties are to be examined. Due to forces between the sharp tip and the sample, cantilever bends in the vertical direction. Bending of the cantilever generates nonzero deflection signal at the output of the detection electronics which is used as a feedback to control the sample height and to maintain a constant base sample separation. Once the vertical control loop reaches to a steady state, XY scanner moves on to the next pixel to be probed. This is the simplest operation of AFM and is called the "static mode". Static mode is similar to scanning probe microscopy (SPM) where the tunnelling current between the conductive sharp tip and the conductive surface is measured to extract the sample topography.

In static mode, the cantilever has to be softer than the force constant of the surface bonds, since the deflection of the lever must be larger than the deformation of the sample. This restricts the stiffness of the lever to a few N m^{-1} [4]. However, the presence of the attractive forces causes the tip of the soft cantilever to suddenly jump into contact, which is called snapping-in, and therefore the irreversible destruction of both the tip and the sample. A static mode AFM also suffers from $1/f$ noise and lateral frictional forces are present making it experimentally challenging to realize.

In dynamic atomic force microscopy, the cantilever is vibrated at or close to its resonance frequency. The tip periodically interacts with the surface and the tip sample forces modulates the properties of the vibration, such as its phase, amplitude or frequency. This modulation is detected, and the feedback electronics adjusts the base sample separation to maintain the constancy of the specific vibration property. In contrast to static mode, soft cantilevers can be used to probe the surface in dynamic force microscopy, since the kinetic energy of the cantilever prevents the tip to snap in to the surface. There are two basic and conventional operation modes of the dynamic atomic force microscopy: amplitude modulation atomic force microscopy (AM-AFM) and frequency modulation atomic force microscopy (FM-AFM).

2.4 Frequency modulation AFM and spring softening

We will be dealing with problems where the properties of a single mode will be of interest. Therefore, in this section and the subsequent two sections we are going to drop indices for effective masses and stiffnesses. Furthermore, the tip-sample distance will be given by $d = Z_0 + z$ where z represents the motion of the mode.

The transfer function of a mode having resonance frequency $\omega_1 = \sqrt{\frac{k}{m}}$, effective mass m, stiffness k and quality factor Q is:

$$\frac{Z(\omega)}{F_{ext}(\omega)} = \frac{w_1^2/k}{(j\omega)^2 + j\frac{\omega_1\omega}{Q} + \omega_1^2} \tag{2.9}$$

This follows directly by taking the Fourier transform of both sides of Eq. 2.2. Notice that for low frequency excitations $F_{ext}(\omega) = kZ(\omega)$, which is a statement of Hooke's law, meaning that the excitation and displacement are in phase. On the other extreme, we have $Z(\omega) = \frac{-\omega_1^2}{k\omega^2}F_{ext}(\omega)$, meaning that for higher frequencies phase shift between vibrations and external excitation converges to 180° and

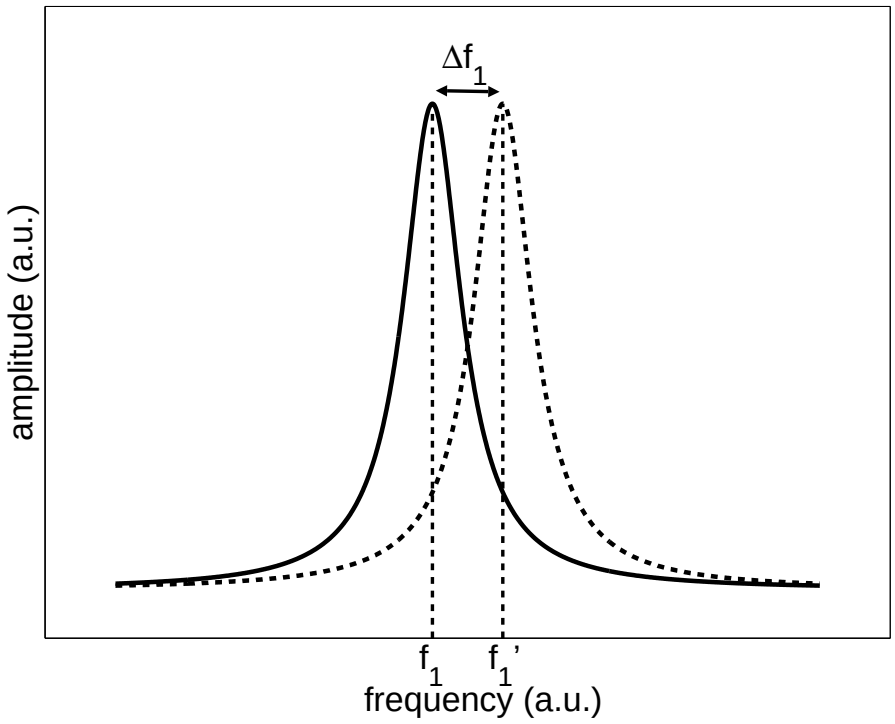

Figure 2.4: Resonance curve for a harmonic oscillator (solid line) and under the influence of a force field (dashed lines). Gradient of the tip sample forces produces a shift of the resonance curve by Δf_1.

vibrating the lever becomes harder. When $\omega = \omega_1$, we have $Z = -j\frac{Q}{k}F_{ext}$, i.e. vibration lags the external excitation by 90° and attains its maximum amplitude. This is the resonance excitation. At resonance, if the excitation is of the form $F_0 \cos(\omega_1 t)$ in the time domain, then the tip trajectory is given by $F_0\frac{Q}{k}cos(\omega_1 t - \phi)$ where $\phi = \frac{\pi}{2}$. Note that the quantity $F_0\frac{Q}{k} = A_0$ is called the free air vibration amplitude.

Up to now we have examined the cases where $F_{ext}(t)$ is sinusoidal, i.e., the tip-sample interaction does not exist. Now suppose that the tip oscillates sinusoidally in a force field with a constant amplitude, i.e., $z = A\cos(\omega t)$. For small oscillation amplitude A, ignoring the DC term, we can approximate the tip-sample force with $F_{ts}(t) = k_{ts}z$ where k_{ts} represents the spring constant or the force gradient

of the interaction. Let us rewrite Eq. 2.2 assuming that $F_{ts}(t) = k_{ts}z$:

$$m\frac{d^2z}{dt^2} + \frac{m\omega_1}{Q}\frac{dz}{dt} + kz = F_{ext}(t) \approx k_{ts}z + F_0\cos(\omega t) \tag{2.10}$$

Subtracting $k_{ts}z$ from both sides of the equation we get:

$$m\frac{d^2z}{dt^2} + \frac{m\omega_1}{Q}\frac{dz}{dt} + (k - k_{ts})z = F_0\cos(\omega t) \tag{2.11}$$

This is the "spring softening" effect. Observe that the resonance characteristics of the mode is disturbed, i.e., a small oscillation in a force field effectively modulates the resonance frequency of the eigenmode. For systems with sufficiently large Q the new/perturbed resonance frequency f_1' is given by:

$$f_1' = \frac{1}{2\pi}\sqrt{\frac{k - k_{ts}}{m}} = f_1\sqrt{1 - \frac{k_{ts}}{k}} \tag{2.12}$$

If the force gradient k_{ts} is positive, the resonance frequency shifts to smaller values. On the other hand, if the force gradient is negative, the resonance frequency becomes greater. Fig. 2.4 shows the shift of the resonance curve by Δf_1. For small frequency shifts Eq. 2.12 reduces to $f_1' \approx f_1(1 - \frac{k_{ts}}{2k})$, therefore the frequency shift is:

$$\Delta f_1 = f_1' - f_1 \approx -f_1 k_{ts}/2k \tag{2.13}$$

Notice that for modes with larger spring constants the effect becomes negligible.

For a large A, the tip-sample force cannot be approximated by a simple function of z. However, using harmonic approximation the frequency shift can be calculated by the formula [18]:

$$\Delta f_1 \approx -\frac{f_1^2}{kA}\int_0^{1/f_1} F_{ts}(t)cos(2\pi f_1 t)\, dt \tag{2.14}$$

This implies that the average force gradient experienced by the tip is calculated simply by projecting the tip-sample force onto the fundamental vibration and this is used to derive the frequency shift. We present the derivation of Eq. 2.14 in Appendix A. Notice that the frequency shift depends on the aggregate effect of the tip sample forces, therefore frequency modulation AFM is only sensitive

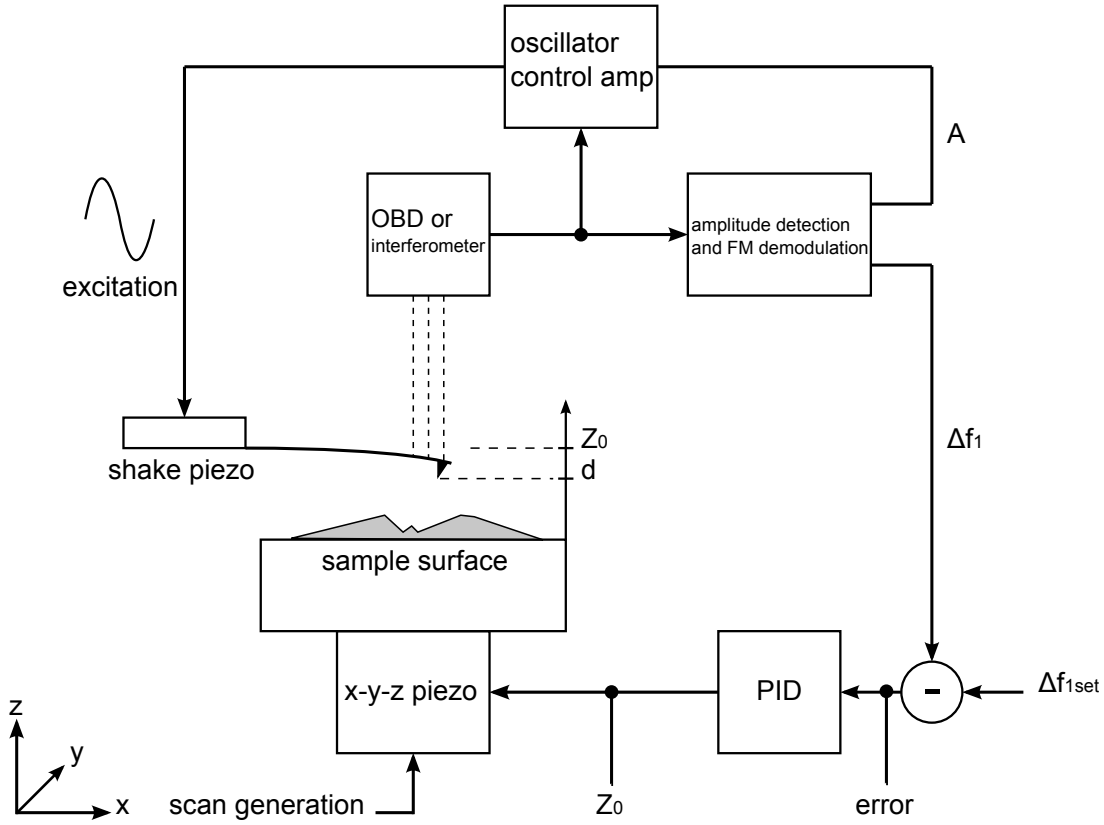

Figure 2.5: Schematic description of the single mode FM-AFM operation.

to large features of the tip-sample forces and therefore —if additional information channels are not present— primarily to surface topography. Note that using Eq. 2.13 and Eq. 2.14 we can now define the average force gradient $\langle k_{ts} \rangle$ experienced by the tip as:

$$\langle k_{ts} \rangle = \frac{2}{A} \frac{1}{T_1} \int_0^{T_1} F_{ts}(t) cos(2\pi f_1 t)\, dt \tag{2.15}$$

where $T_1 = 1/f_1$ is the period of the oscillation.

In FM-AFM typically the first flexural mode of a cantilever with natural resonance frequency f_1 is driven on positive feedback such that the oscillation amplitude A stays constant. Fig. 2.5 shows a schematic description of the technique. The deflection signal enters into oscillator control amplifier and is band pass filtered and 90° of phase shift is introduced. The output of the phase shifter

is multiplied by $-g$ and is used to drive the cantilever, where a square law detector calculates the oscillation amplitude for the adjustment of the gain g. That is, drive amplitude F_0 is not fixed, but is modulated and used to compensate for the lost energy to maintain constant vibration amplitude A. Total phase shift on the feedback loop adds up to 270°. At the resonance frequency of the cantilever, i.e., at the frequency where the transfer function of the cantilever has the highest gain, the phase between the drive and the oscillation is 90°. Therefore, the cantilever starts oscillating at its resonance, where the total phase adds up to 360°. The oscillation frequency f_1' depends on the strength of the force field within which the cantilever is vibrating. The frequency deviation Δf_1 from cantilever's natural resonance frequency f_1 is described by Eq. 2.13 for small A or Eq. 2.14 for large A. Frequency shifts are demodulated to extract Δf_1 and an additional feedback loop adjusts the base sample separation Z_0 such that frequency shift Δf_1 also stays constant. This is called the topographic mode and similar variants exist such as "constant height imaging" or "constant excitation imaging" where observables are different, however same principles also apply to them.

It is a very important property of FM-AFM that readout speed and imaging bandwidth is not limited with the finite Q of the cantilever, since the frequency shifts occur instantaneously. Readout speed is limited by the controller performance, the detection bandwidth of the FM demodulator and the signal to noise ratio. Therefore, FM-AFM is usually used in high vacuum environments where the quality factor of the cantilever is very large [19].

2.5 Amplitude modulation AFM

In AM-AFM cantilever is driven at a fixed frequency which is usually near to the resonance frequency f_1 of the first flexural mode with quality factor Q and

stiffness k. Cantilever starts to vibrate with an initial amplitude A_0 and phase ϕ (with respect to the drive). When the tip interacts with the surface, conservative and non-conservative forces cause the amplitude and the phase of the vibration to change. The change is not instantaneous, since the quality factor of the cantilever, although being finite, is much larger than one. Vibration amplitude is detected and the feedback electronics adjusts the base sample separation Z_0 to maintain a fixed vibration amplitude of A_{set}. The change in amplitude settles with a time constant of $\tau = 2Q/f_1$, if the feedback bandwidth is large enough. See Fig. 2.6 for a schematic description of the method.

The dynamics can be formulated by a second order nonlinear differential equation:

$$m\frac{d^2z}{dt^2} + \frac{m\omega_1}{Q}\frac{dz}{dt} + kz = F_{ts}(t) + F_0\cos(\omega t) \tag{2.16}$$

If the driven mode is sufficiently high-Q and nonlinear forces acting on the tip are small enough we can use the harmonic approximation. The harmonic approximation to the problem requires that the tip motion is essentially sinusoidal, i.e., higher order vibrations at integer multiples of f_1 are sufficiently small to be neglected. Usually this is the case and without loss of generality tip motion is of the form $z = A(Z_0)\cos(\omega t - \phi(Z_0))$, i.e., for different base sample separations, there exists a vibration amplitude and phase with respect to drive, however motion remains to be sinusoidal. A mathematical description of the underlying physics of AM-AFM has to relate experimental parameters to observables such as vibration amplitude and phase. Numerical solutions for $A(Z_0)$ and $\phi(Z_0)$ depending on F_{ts} and cantilever properties (f_1, k, Q) are available. Obtaining closed form expressions are also desirable, however this is a nontrivial task. This is surprising since the technique is seemingly simpler than the frequency modulation AFM which turns out to be analytically accessible.

Paulo and Garcia derived closed form expressions by applying energy conservation and the virial theorem to the problem [20, 21]. The virial theorem states

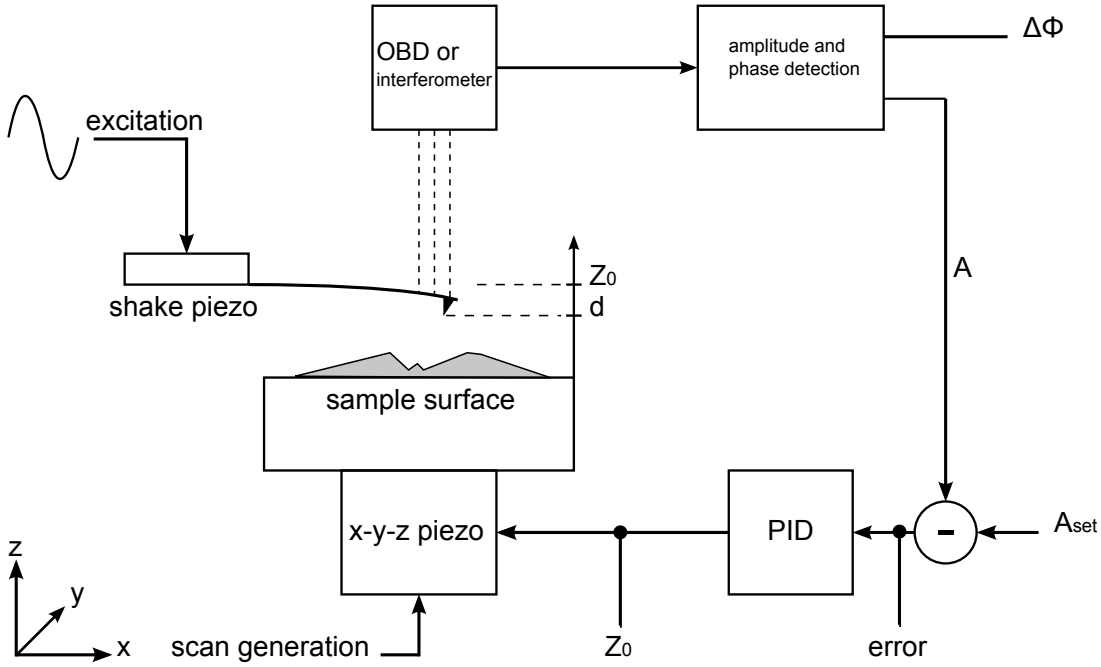

Figure 2.6: Schematic description of the single mode AM-AFM operation.

that average kinetic energy of the motion is equal to minus the half of the average potential energy $\langle K \rangle = -1/2\langle F \cdot z \rangle$, where $\langle F \cdot z \rangle = 1/T \oint F(t) z dt$ and T is the oscillation period $1/f_1$. Applying the virial theorem to Eq. 2.16 and assuming that $z = A(Z_0)\cos(\omega t - \phi(Z_0))$ we get:

$$\cos\phi \approx -\frac{2Q\langle F_{ts} \cdot z \rangle}{kAA_0} \tag{2.17}$$

with the assumption that $\omega \approx \omega_1$, the average cantilever deflection is close to zero, and the free vibration amplitude is $A_0 = F_0 Q/k$. A second identity can be derived from the consideration that in the steady state, the average power supplied to tip P_{in} must be equal to the sum of average dissipated power by hydrodynamic and tip-sample forces, P_{med} and P_{ts} respectively, i.e., $P_{in} = P_{med} + P_{ts}$ [22]. The average power supplied to the tip is the driving force times the tip velocity averaged over an oscillation cycle, $P_{in} = \langle F_d \cdot z' \rangle$ where $F_d = F_0 \cos\omega t = A_0 k/Q \cos\omega t$. The average dissipated hydrodynamic power is the hydrodynamic force times the tip velocity averaged over an oscillation cycle $P_{med} = \langle F_{med} \cdot z' \rangle$ where hydrodynamic forces are $F_{med} = m\omega_1/Q z'$. Similarly, the average

dissipated power by the tip-sample force is $P_{ts} = \langle F_{ts} \cdot z' \rangle$. Combining these we arrive at:

$$\sin\phi \approx \frac{A}{A_0} + \frac{2QP_{ts}}{kAA_0\omega_1} \tag{2.18}$$

Notice that phase shift is not independent from the oscillation amplitude, while on the other hand nonconservative interactions modulates ϕ such that dissipative properties of the tip sample interaction can be recorded. Although phase modulation due to dissipative tip sample interactions is a significant effect (see Appendix B), the tip has to experience repulsive forces (i.e. tip has to be in contact with the surface) in order to obtain phase contrast which is not desirable for imaging delicate samples such as organic molecules.

Combining Eq. 2.17 and Eq. 2.18 allows us to derive a relationship for the oscillation amplitude:

$$A \approx \frac{A_0}{\sqrt{2}} \left(1 - \frac{2P_{ts}}{P_{med}} \pm \sqrt{1 - \frac{4P_{ts}}{P_{med}} - 16 \left(\frac{\langle F_{ts} \cdot z \rangle}{F_0 A_0} \right)^2} \right)^{1/2} \tag{2.19}$$

where $P_{med} = \omega_1 k A_0^2 / 2Q$. We are going to investigate conservative interactions for $P_{ts} = 0$. In such a case, the above equation implies that the oscillation amplitude A is given by the positive real roots of a fourth order polynomial:

$$A^4 - A^2 A_0^2 + \frac{4A_0^2}{F_0^2} \langle F_{ts} \cdot z \rangle^2 = 0 \tag{2.20}$$

We remark that the positive real solutions for A provided a fixed $\langle F_{ts} \cdot z \rangle^2$ is not necessarily unique. This is the case, since an amplitude modulation AFM is bistable in nature. There exists repulsive and attractive solutions. Initially only attractive solutions are physically realizable. As the base sample separation is decreased system continues to prefer attractive solutions until a critical point is reached. After a critical base sample separation, the repulsive solutions for the oscillation amplitude has to be realized. The bistability can cause different base sample separations to correspond to a single set point of oscillation amplitude A_{set}, therefore has to be avoided by proper selection of the excitation frequency, amplitude and the set point.

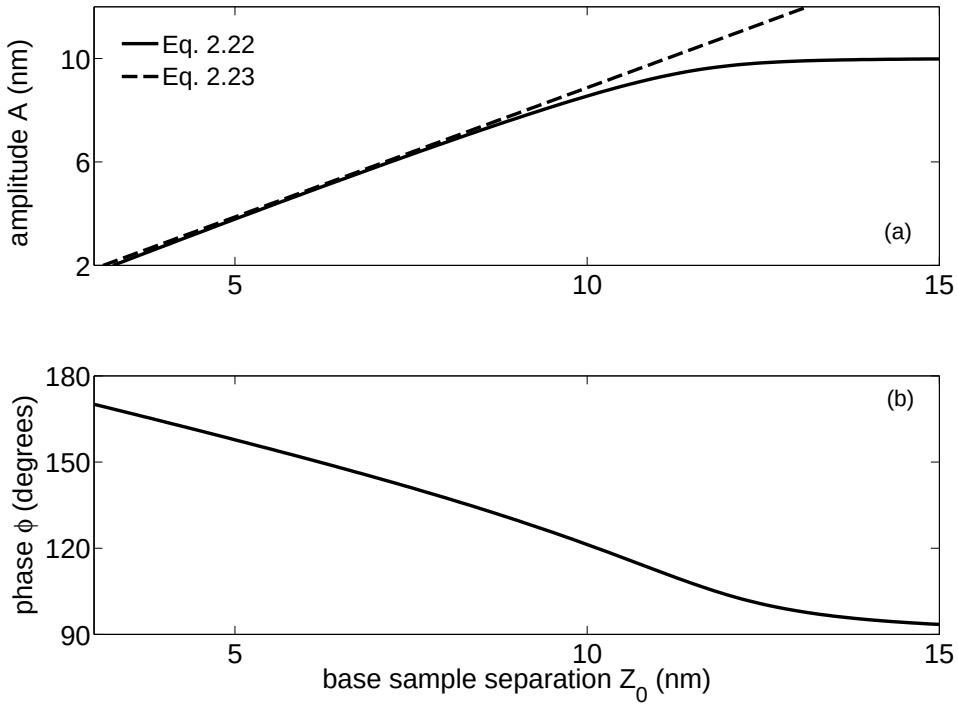

Figure 2.7: (a) Vibration amplitude A calculated from Eq. 2.22 (solid line) and calculated from Eq. 2.23 (dashed line) (b) phase ϕ calculated from Eq. 2.18 with respect to the base sample separation Z_0. $A_0 = 10$ nm, $Q = 250$, $k = 1$, $R = 10$ nm, $H = 10 \cdot 10^{-20}$.

Closed form expressions for A exists if only oscillations remain in the attractive regime. For example, the repulsive solutions can be suppressed by choosing small A_0. Indeed, biological bodies can easily be damaged if the tip spends time in the repulsive regime and imaging delicate samples in the attractive regime is preferred. Therefore, assuming attractive solutions and that the tip sample interaction is given by Eq. 2.8, $\langle F_{ts} \cdot z \rangle$ can be expressed as:

$$\langle F_{ts} \cdot z \rangle = \frac{1}{T} \oint \frac{-HRA\cos(\omega_1 t)}{6(Z_0 + A\cos(\omega_1 t))^2} dt = \frac{HRA^2}{6\sqrt{(Z_0^2 - A^2)^3}} \tag{2.21}$$

Combining Eq. 2.20 and Eq. 2.21 we arrive at an eighth order polynomial:

$$A^8 - (A_0^2 + 3Z_0^2)A^6 + (3A_0^2Z_0^2 + 3Z_0^4)A^4 - (3A_0^2Z_0^4 + Z_0^6 + K)A^2 + A_0^2Z_0^6 = 0 \tag{2.22}$$

where $K = Q^2H^2R^2/9k^2$. The oscillation amplitude A corresponding to a fixed Z_0 is given by the positive real root of the above polynomial and there exists

only one such root although we do not have the proof. An asymptotical (true for some $Z_0 < A_0$) but useful solution to Eq. 2.22 is given by:

$$A = Z_0 - \left(\frac{Q^2 H^2 R^2}{45 k^2 A_0^3} \right)^{1/3} \tag{2.23}$$

We do not show how Eq. 2.23 is derived, since this is rather cumbersome. In Fig. 2.7 we see the vibration amplitude A calculated from Eq. 2.22 and Eq. 2.23, and phase ϕ calculated from Eq. 2.18 with respect to the base sample separation Z_0.

Similar to FM-AFM, amplitude and phase changes in AM-AFM are dependent upon averaged quantities of the tip sample interaction (see Eq. 2.20). In the absence of dissipative tip sample interactions, AM-AFM is only sensitive to topographical features of the sample surface. Without going any further let us stress this point one more time. Conventional force microscopy techniques are dominantly sensitive to topographical features in the absence of additional information channels. A cantilever tip which is located away from the surface can detect surface forces, however cannot distinguish them from the topographical variation. Therefore, single mode amplitude and frequency modulation AFM techniques are primarily used to investigate the surface topography. Indeed, the presence of compositional heterogeneity deteriorates the performance of the two widely used methods.

2.6 Sensitivity and noise in AFM

Thermal energy in each mode of a cantilever can be calculated using equipartion theorem. Equipartition theorem from statistical mechanics states that each and every one of the degrees of freedom of a system has a kinetic energy proportional to the absolute temperature of the thermal bath with which the system is in statistical equilibrium. Proportionality constant is the Boltzmann constant

multiplied by 1/2. Therefore mean square vibration amplitude in the vertical direction of an eigenmode represented by a mass-spring system is given by the relation [11]:

$$\frac{1}{2}k_BT = \frac{1}{2}m\langle z'^2\rangle = \frac{1}{2}k\langle z^2\rangle \tag{2.24}$$

where k_B is the Boltzmann constant, T is the absolute temperature, k is the stiffness of the mode. The mean square vibration amplitude $\langle z^2\rangle$ can be used to calculate the force noise power spectral density S_f since:

$$\langle z^2\rangle = \int_0^\infty |G(f)|^2 S_f df \tag{2.25}$$

where $G(f)$ is the transfer function of that mode. We assume that force noise power spectral density is white and that the transfer function of the eigenmode assumes a Lorentzian shape (see Eq. 2.9). In such a case, combining Eq. 2.24 and Eq. 2.25 yields:

$$S_f = \frac{4kk_BT}{\omega_1 Q} \tag{2.26}$$

Within a reception bandwidth of B, the force noise RMS amplitude is then given by:

$$F_{min} = \sqrt{S_f B} = \sqrt{\frac{4kk_BTB}{\omega_1 Q}} \tag{2.27}$$

F_{min} is the minimum detectable force and determines the ultimate force sensitivity achievable by cantilevered beams and static mode atomic force microscopy.

For dynamic atomic force microscopy techniques one speaks of sensitivity to force gradient. In the light of Eq. 2.27 the minimum detectable force gradient is given by:

$$k_{ts}^{min} = \sqrt{\frac{4kk_BTB}{\omega_1 QA^2}} \tag{2.28}$$

where A is the oscillation amplitude. Eq. 2.28 is true for both AM-AFM and FM-AFM (the case for FM-AFM is complicated, more on this point later). Any improvement in k_{ts}^{min} means improved lateral and vertical resolution in dynamic force microscopy. We remark that this analysis neglects the noise contribution

due to optical or piezoresistive deflection sensors and subsequent detection electronics.

Notice the appearance of conflicting terms in Eq. 2.27. Low stiffness implies lower resonance frequencies and typically a small quality factor. For rectangular cantilevers resonance frequency over stiffness ratio is a function of the dimensions and material properties of the cantilever, while quality factor in vacuum is predominantly determined by the intrinsic volume dissipation within the material. Theoretical and experimental analyses have shown that ultimate force sensitivity in vacuum is achievable by using thin, narrow and long cantilevers [11]. A similar analysis for cantilevers suspended in air shows that hydrodynamic damping due to air friction determines the quality factor, and for ultimate sensitivity a thin, narrow and short cantilever (therefore with high resonance frequency) has to be used [23].

In AM-AFM, bandwidth of the detection electronics can be as large as $B = f_1/Q$, therefore increasing the quality factor of the probe by means of using ultra-small cantilevers or suspending the probe in vacuum in order to achieve higher force sensitivity implies slower scan speeds. Indeed, a double fold improvement of the quality factor brings $\sqrt{2}$ fold improvement of the force sensitivity, however brings a two times longer imaging duration. In FM-AFM bandwidth can be chosen arbitrarily large independently from the numerical value of the quality factor. This is possible since frequency shifts in FM-AFM are instantaneous. Therefore FM-AFM seems to be a better candidate for high speed imaging.

Finally, let us write down the measurement ambiguities of amplitude and phase in the presence of thermal noise. If the minimum detectable force is given by Eq. 2.27, then the minimum detectable amplitude δA is obtained by multiplying F_{min} with the gain of the harmonic oscillator at resonance frequency:

$$\delta A = F_{min}\frac{Q}{k} = \sqrt{\frac{4k_BT}{k}} \tag{2.29}$$

For soft cantilevers δA is on the order of a few Angstroms. Similarly phase ambiguity $\delta\phi$ can be roughly estimated to be:

$$\delta\phi = \frac{\delta A}{A} \tag{2.30}$$

For an oscillation amplitude of 50nm, $\delta\phi$ is on the order of 0.1°.

2.7 Challenges in AFM

AFM has several experimental challenges and a successful realization of it requires great expertise.

Non-monotonic tip sample forces make it difficult to establish a vertical feedback loop. Van der Waals forces and attractive chemical forces can cause jump-to-contact, causing instabilities manifested by artifacts in the imaging signal [24]. Dynamic force microscopy methods were introduced in order to overcome the problem [25]. The stability can be increased by using large amplitudes and stiff cantilevers at the expense of vertical resolution.

The presence of the long range forces means that the tip is sensitive to integral features in the lateral direction. This causes a blurring in the imaging signal. Therefore, for ultimate lateral resolution it is necessary to be sensitive primarily to short range forces that vary at the atomic scale.

In AFM, the forces are measured by the deflection of the cantilever. The noise sources are thermomechanical noise of the cantilever, $1/f$ noise which is increasingly dominant at low frequencies, detection noise which includes laser shot noise, phase noise and the pointing noise [26], and vibrations between the mechanical structures of the system. For highly sensitive and high resolution imaging all noise sources has to be taken into consideration and has to be minimized.

Scan speed in AFM is limited by the slowest component on the feedback loop [27]. High performance controllers [28], z-axis actuators with large bandwidth [29], small cantilevers with high resonance frequency [30] are introduced to achieve higher frame rates. However, slow transient response of the probe with a large quality factor is a fundamental restriction on the available bandwidth [27]. Frequency modulation AFM [19] seems to circumvent this problem since the frequency shift of the vibration is almost instantaneous and is independent of the quality factor of the resonator, however, frequency detectors with bandwidths limited to a few kHz restricts the scan speed of frequency modulation techniques.

Amplitude and frequency modulation AFM are only sensitive to large features of the tip-sample interaction. Therefore, amplitude or frequency shifts are sensitive to topographical features of the sample surface. Moreover, compositional variations may also interfere with the topographical signal, i.e., without additional information channels it is impossible to differentiate the surface stiffness information from the topographical signal. Bimodal excitation or harmonic imaging, which are discussed in the next chapter, opens up the possibility of simultaneous and fast acquisition of the contact properties.

Chapter 3

FORCE MICROSCOPY TECHNIQUES TO ACHIEVE COMPOSITIONAL CONTRAST

3.1 Bimodal AM-AFM

In a single mode AM-AFM, the first flexural mode is excited and the surface is imaged while the feedback electronics adjusts the base-sample separation to maintain a constant oscillation amplitude. The phase shift between the drive and the oscillation reveals information on dissipative mechanisms, i.e., higher dissipated energy during tip sample interaction implies larger phase shifts. However, repulsive forces applied on surfaces to achieve reasonable phase contrast above the noise floor may cause irreversible damage to the sample surface.

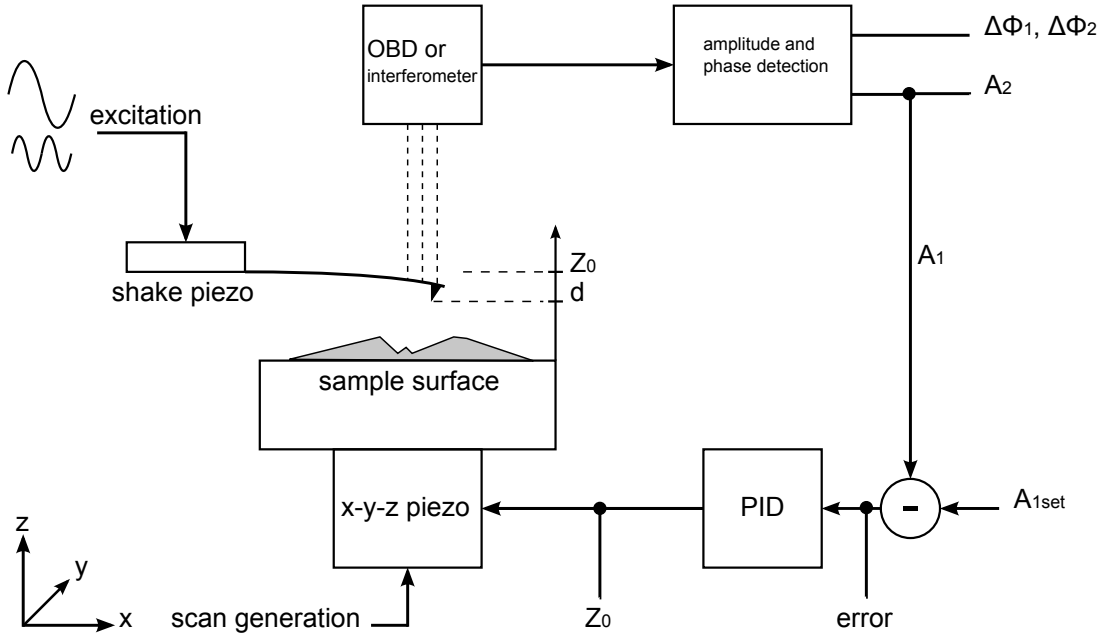

Figure 3.1: Schematic description of the bimodal AM-AFM operation.

Simultaneous excitation of the first flexural mode and a higher mode was proposed by Garcia. In this method, the first mode is operated as in the single mode AM-AFM, and the oscillation amplitude A_1 of the first mode is used to image topography. The higher mode is driven at its resonance frequency f_2 with a constant excitation and phase shift ϕ_2 between the drive and the oscillation is recorded. See Fig. 3.1 for a schematic description of bimodal AM-AFM operation. It is reported by several groups that ϕ_2 is highly sensitive to contact properties even in the nondissipative regime of the tip sample interaction. This increased sensitivity allows users to obtain compositional features using gentle forces as low as $10 - 100$ pN [31].

Using bimodal AM-AFM Martinez *et. al.* imaged sexithienyl (T6) molecules deposited on silicon, and achieved a phase contrast of $\Delta\phi_2 = 1°$, enhanced by a factor of 10 compared to $\Delta\phi_1 = 0.1°$ which was barely over the noise floor ($0.05°$) [7]. Patil et. al. succeeded to identify different components of the protein chains. They imaged a Y-shaped IgG antibody deposited on mica and two of

the fragments showed a phase shift of 8°, while the other showed a phase shift of 5°, therefore managed to identify different sites on an organic molecule [8].

A mathematical understanding of the enhanced sensitivity of bimodal operation is nontrivial, because one has to solve for steady state values of $A_1(Z_0)$, $\phi_2(Z_0)$ simultaneously in terms of cantilever properties (f_1, k_1, Q_1; f_2, k_2, Q_2) and the free air vibration amplitudes of the modes (A_{10}, A_{20}), using two second order differential equations describing motion of the tip, coupled by a nonlinear force interaction described by the Hamaker constant. Lozano *et. al.* applied the virial theorem and the energy conservation principles to each of the modes and concluded that [9]:

$$A_2 = A_{20} \sin \phi_2 \tag{3.1}$$

where

$$\phi_2 = \arctan \frac{1 \pm \sqrt{1 - (4v_2)^2}}{4v_2} \tag{3.2}$$

given

$$v_2 = \frac{Q_2}{k_2 A_{20}^2} \frac{1}{T} \int_0^T F_{ts}(t) A_2 \cos(2\pi f_2 t) dt \tag{3.3}$$

where $F_{ts}(t) = F_{ts}(Z_0 + A_1 \cos(2\pi f_1 t) + A_2 \cos(2\pi f_2 t))$, $T = p_1/f_1 = p_2/f_2$ for some integers p_1 and p_2 such that $A_1 \cos(2\pi f_1 t) + A_2 \cos(2\pi f_2 t)$ is periodic, and A_1 is given by:

$$A_1 = A_{10} \sin \phi_1 \tag{3.4}$$

where

$$\phi_1 = \arctan \frac{1 \pm \sqrt{1 - (4v_1)^2}}{4v_1} \tag{3.5}$$

given that

$$v_1 = \frac{Q_1}{k_1 A_{10}^2} \frac{1}{T} \int_0^T F_{ts}(t) A_1 \cos(2\pi f_1 t) dt \tag{3.6}$$

Notice that above treatment is the bimodal equivalent to the analysis presented in Sec. 2.5, and is reformulated in terms of phase shifts.

The sensitivity of ϕ_2 to the features of tip sample forces is described by Eq. 3.3. The cantilever oscillates at fixed base sample separation regardless of

the surface topography, and since the higher mode is not controlled by feedback, A_2 and ϕ_2 are free to change on surfaces with different contact properties. Therefore, these two parameters serve as additional information channels for acquiring compositional contrast. We remark that A_2 and ϕ_2 are coupled to each other as in single mode AM-AFM, i.e., they are not independent (see Eq. 3.1). We postpone the discussion of the reasons for the increased sensitivity to Chapter 5 where we develop mathematical tools which will help us with the interpretation.

Although bimodal operation was developed for the amplitude modulation mode, Kawai *et. al.* used simultaneous excitation of two flexural modes in a frequency modulation scheme where the amplitude of the modes stay constant. They concluded that the frequency shift of the higher mode was proportional to force gradient averaged over the large oscillation of the first mode, leading to enhanced sensitivity to topographical features [32].

3.2 Harmonic Imaging

During non-linear tip sample interactions in AM-AFM, higher harmonics, causing anharmonic tip motions, are also generated at the integer multiples of the tapping frequency f_1. One of the earliest works on harmonic imaging indicates that anharmonic oscillations, although they are 1% of the harmonic oscillation, can be used to obtain image contrast based on contact stiffness [33].

Understanding the increased sensitivity of the harmonic imaging to contact properties is relatively easy. The tip-sample interaction force, $F_{ts}(t)$, can be roughly estimated by a pulse wave with period $1/f_1$ and a width equal to the contact time, T_c. The Fourier transform of $F_{ts}(t)$ is an impulse train with period f_1 modulated by a sinc envelope such that the first zero crossing at of $F(f)$ is at $1/T_c$. Usually the contact time occupies a small fraction of the tapping period

and a stiff interaction means a smaller T_c therefore a wider spread of $F(f)$. On the other hand, the spectrum of the tip motion $H(f)$ is given by the product of the transfer function of the cantilever with the Fourier transform of the tip sample interaction, $H(f) = G(f) \cdot F(f)$. It turns out that $H(f)$ is also a impulse train with period f_1. Impulses at the spectrum of the tip motion are called the harmonics of the vibration. After detecting the vibrations of the tip by solving the inverse problem (i.e. multiplying $H(f)$ with $1/G(f)$ and taking the inverse Fourier transform) one can obtain tip sample interaction $F_{ts}(t)$.

As it is the case in other variations of AM-AFM, the base-sample separation in harmonic imaging is adjusted in such a way that the first component or the first harmonic of $H(f)$, which is the amplitude of the first mode vibrations, is kept constant so that A is always equal to A_{set}. This ensures that the recovery of the tip sample interaction is unambiguous, in other words, the base-sample separation is kept constant independently from the surface topography. Eventually, $F(f)$ is characterized by a constant amplitude sinc function, albeit the location of the first zero crossing is modulated depending on the stiffness of the interaction. See Fig. 3.2 for a comparison of interactions with a stiff and a compliant surface. Notice that for frequencies smaller than $1/T_c$ harmonics of the stiff interaction are larger. Therefore, instead of recovering the full spectrum of harmonics, one can also lock in to one of the frequencies at an integer multiple of f_1 to acquire surface stiffness information.

The challenge in harmonic imaging is that higher frequency excitations at the integer multiples of f_1 corresponds to a regime of the transfer function of the rectangular cantilever where gain drops proportional to f^2. This is why harmonic content of the tip trajectory is usually small. Furthermore, if the excited anharmonic motion is below a certain threshold it is impossible to recover it due to the presence of the detection noise. That is, the signal is buried under the noise floor.

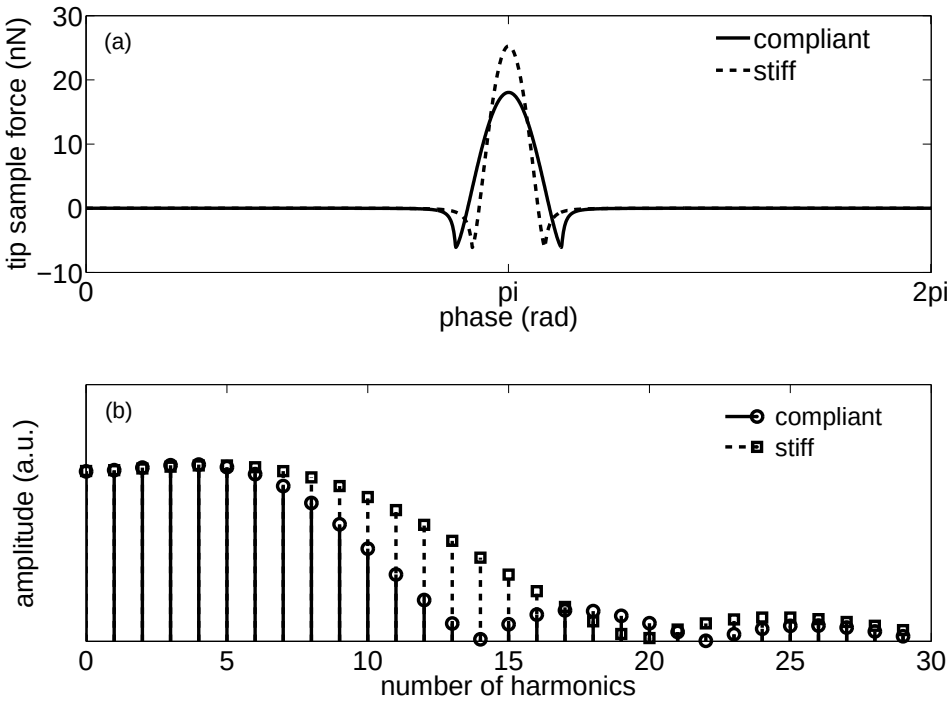

Figure 3.2: (a) Tip sample interaction with respect to time (b) Fourier transform (harmonics) of the tip sample interaction. $H = 10 \cdot 10^{-20}$, $R = 10$ nm, $a_0 = 0.165$ nm, $A_0 = 20$ nm, $A_{set} = 9$ nm, $k_1 = 2.6$, $Q_1 = 100$, $f_T \approx 16 f_1$, $Q_T = 800$, $k_T = 500$. $E = 40$GPa for dashed lines and $E = 10$ GPa for solid lines.

To tackle this problem Balantekin *et. al.* used an excitation frequency of $f_1/3$. Hence 3^{rd} harmonic amplitude could be enhanced by a factor of Q_1 using the first flexural mode's resonance [34]. It is also possible to manufacture cantilevers with a higher order flexural mode that is designed to be resonant at an integer multiple of f_1. Such specific probes are called harmonic cantilevers. More information on harmonic cantilevers can be found in [35].

Torsional harmonic cantilevers, invented by Sahin *et. al.*, provides a means to simultaneously acquire a large number of harmonics generated by nonlinear interaction [6]. A torsional cantilever is a T shaped probe with a tip placed asymmetrically from the long axis. The torsional mode has a resonance frequency f_T and quality factor Q_T. Higher harmonics excite the torsional bending motion

while flexural vibration is used to map topography. Relatively soft spring constant k_T of the torsional mode and the large bandwidth provided by f_T makes the method suitable for recovering harmonics with a high time resolution.

Chapter 4

FORCE SPECTROSCOPY USING BIMODAL FREQUENCY MODULATION FORCE MICROSCOPY

We propose a fast force-spectroscopy technique in which two modes of a cantilever, having resonant frequencies [1] $\bar{f}_1$ and $\bar{f}_2$, are excited such that the amplitudes of both components of the vibration (A_1, A_2) stay constant. Such operation of force microscopy is possible using two separate positive feedback loops which introduce 90° of phase lag between the components of the bi-harmonic vibration of the tip and the excitation at the base. Moreover, two automatic gain circuitries (AGC) which control the gain of the loops to ensure resonance tracking are needed. We measure the instantaneous frequency shift of the second mode from which the tip-sample force gradient can be determined.

[1] In this chapter, the resonance frequency of an eigenmode is represented with a bar over f. For example the resonance frequency of the first mode is $\bar{f}_1$, while instantaneous frequency is simply f_1.

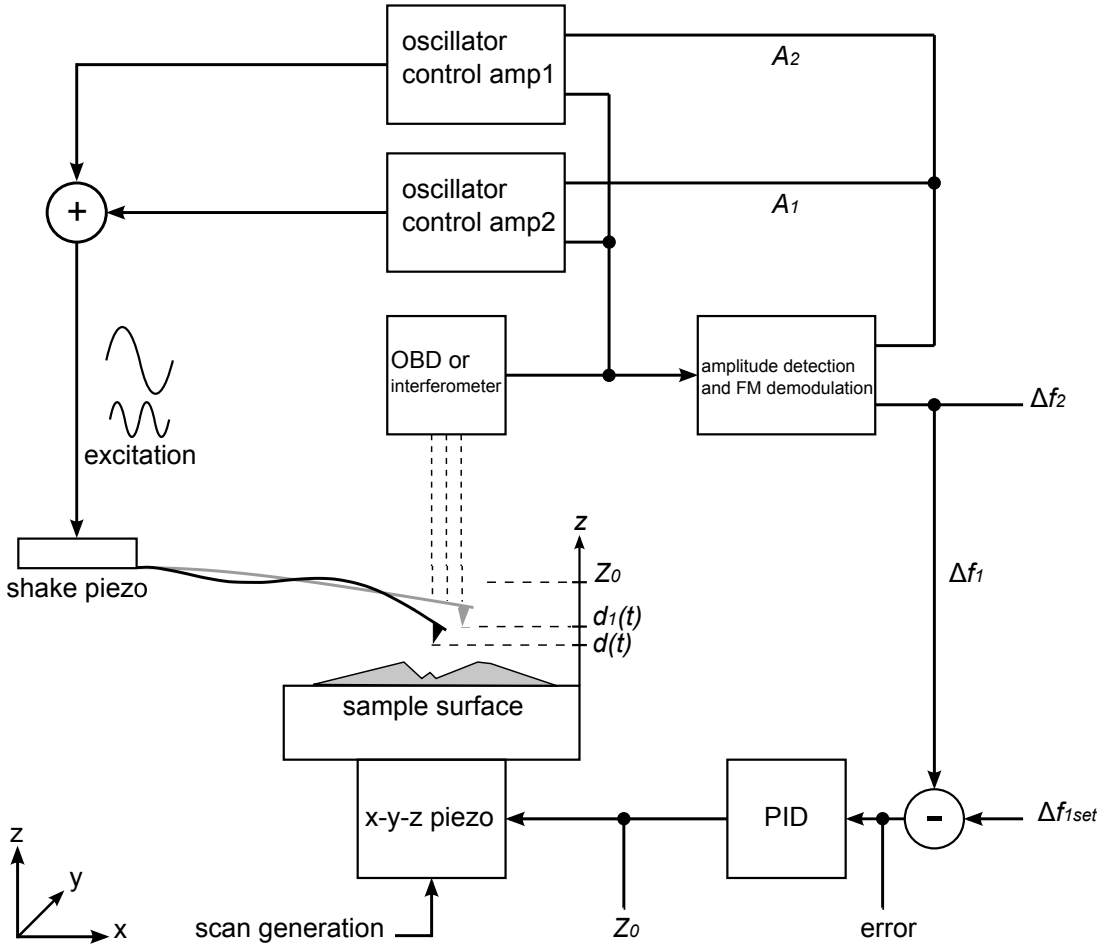

Figure 4.1: Schematic description of the proposed technique. Two modes of a cantilever driven simultaneously. $d(t)$ is the instantaneous tip position with respect to the sample and $d_1(t)$ represents first mode vibrations.

Referring to Fig. 4.1 the instantaneous tip-sample distance, $d(t)$, is written as

$$d(t) = d_1(t) + A_2 \cos(2\pi f_2 t - \phi) \tag{4.1}$$

with

$$d_1(t) = Z_0 + A_1 \cos(2\pi f_1 t), \tag{4.2}$$

where Z_0 is the base-sample (or the average tip-sample) separation, f_1 and f_2 are the instantaneous frequencies of the components of the bi-harmonic vibration centered around $\bar{f}_1$ and $\bar{f}_2$ with ϕ being the phase shift between them. $z_1(t) = A_1 \cos(2\pi f_1 t)$ and $z_2(t) = A_2 \cos(2\pi f_2 t)$ represent the motion of the individual

modes. See Fig. 4.3 for a visualization of the variables describing the motion of the tip.

As the base-sample separation Z_0 is decreased, the tip enters into a force field, i.e., the cantilever tip starts spending time at the attractive and repulsive force regimes for increasingly longer intervals within the period $T_1 = 1/\bar{f}_1$. The presence of the force field modulates the instantaneous frequencies of vibration modes. As it is traditionally exploited in single mode FM-AFM experiments [19], the frequency shift of the first mode ($\Delta f_1 = f_1 - \bar{f}_1$) is sensitive to topographical features, whereas the frequency shift of the higher mode ($\Delta f_2 = f_2 - \bar{f}_2$) is sensitive to compositional features [36]. However, the exact nature of the relation between Δf_2 and the nonlinear tip-sample interaction is complicated, therefore deserves a careful treatment.

4.1 Theory

The frequency shift, Δf_2, due to nonlinear tip-sample interaction can be calculated by a first order perturbation theory using Hamilton-Jacobi approach [3]:

$$\Delta f_2(t) \approx -\frac{\bar{f}_2^{\,2}}{k_2 A_2} \int_{t-\frac{T_2}{2}}^{t+\frac{T_2}{2}} F_{ts}\left(d_1(\tau) + A_2\cos(2\pi\bar{f}_2\tau - \phi)\right)\cos(2\pi\bar{f}_2\tau - \phi)\,d\tau \tag{4.3}$$

where k_2 is the spring constant of the higher mode, $T_2 = 1/\bar{f}_2$ is the period of faster oscillation, and $F_{ts}(d)$ is the force acting on the tip. Note that above equation is a generalization of Eq. 2.14. The frequency shift bears some ambiguity depending on the phase of the samples taken from $\Delta f_2(t)$. Fig. 4.2 shows $\Delta f_2(t)$ calculated from Eq. 4.3 for $\phi = 0$ and $\phi = \pi/2$. If the phase shift ϕ between the components of the biharmonic vibration is known (which, in practice, is not possible), this ambiguity could be avoided by sampling frequency shifts at correct places. However ambiguity is systematic and oscillates around zero with a period

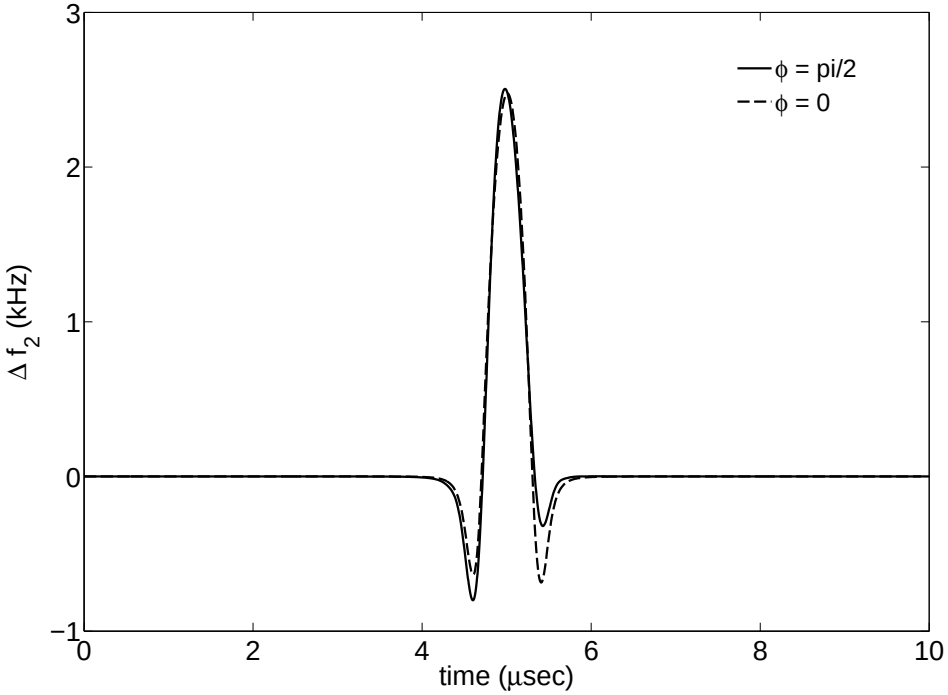

Figure 4.2: Frequency shift of the second mode with respect to time. Solid line is the frequency shift for $\phi = \pi/2$, and dashed line is corrected frequency shift for $\phi = 0$.

of T_2, and it is possible to cancel it simply by sampling $\Delta f_2(t)$ with a period of $T_2/2$ instead of a full period T_2, and averaging out to find the actual value for the frequency shift. Therefore, in what follows, we are going to assume that phase shift ϕ is zero.

We write $d_1(\tau)$ of Eq. 4.2 as a Taylor series expansion of the first order:

$$\begin{aligned} d_1(\tau) &\approx d_1(t) + \left(\frac{d}{d\tau} d_1(\tau)\right)\Big|_{\tau=t} (\tau - t) \\ &= d_1(t) - 2\pi A_1 f_1 \sin(2\pi f_1 t)\ (\tau - t). \end{aligned} \tag{4.4}$$

Assuming that $f_1 \approx \bar{f}_1$ in Eq. 4.4 and through a change of variables $\theta = 2\pi\ \bar{f}_2(\tau - t)$ in Eq. 4.3 we arrive at:

$$\Delta f_2(t) \approx -\frac{\bar{f}_2}{2\pi k_2 A_2} \int_{-\pi}^{\pi} F_{ts}(d_1(t) - A_1 \frac{\bar{f}_1}{\bar{f}_2}\theta \sin(2\pi \bar{f}_1 t) + A_2 \cos\theta) \cos\theta\, d\theta \tag{4.5}$$

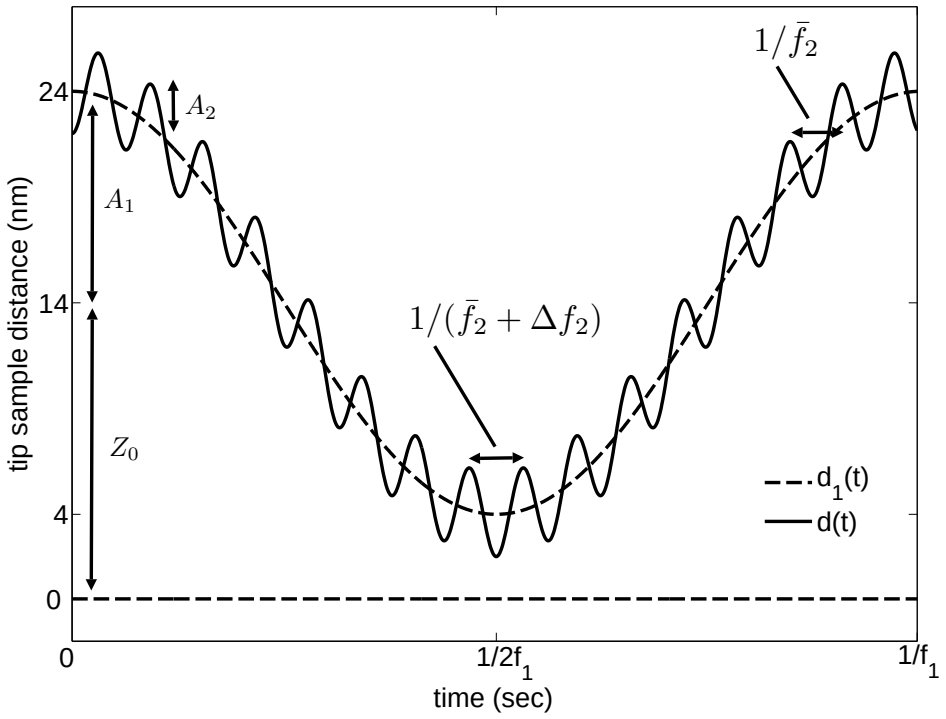

Figure 4.3: Tip trajectory with respect to time during a single period of the first mode vibrations. Base sample separation $Z_0 = 14$ nm, while $A_1 = 10$ nm and $A_2 = 2$ nm.

This integral can be approximated by:

$$\Delta f_2(t) \approx -\frac{\bar{f}_2}{2\pi k_2 A_2} \int_{-\pi}^{\pi} F_{ts}(d_1(t) + A_2 \cos\theta) \cos\theta \, d\theta \,. \tag{4.6}$$

if we have

$$\left| A_1 \frac{\bar{f}_1}{\bar{f}_2} \theta \sin(2\pi \bar{f}_1 t) \right| \ll |A_2 \cos\theta| \tag{4.7}$$

for all t and θ. We note that the frequency shift Δf_2 is significant only during the "contact time" (T_c), given by:

$$\frac{2n+1}{2f_1} - \frac{T_c}{2} < t < \frac{2n+1}{2f_1} + \frac{T_c}{2} \tag{4.8}$$

If T_c is small enough, we have $|\sin(2\pi \bar{f}_1 t)| < 2\pi \bar{f}_1 T_c/2$, hence the requirement in Eq. 4.7 becomes:

$$\pi^2 A_1 \frac{\bar{f}_1^{\,2}}{\bar{f}_2} T_c \ll A_2. \tag{4.9}$$

We remark that the condition in Eq. 4.9 corresponds to an operating regime for which the bi-harmonic system starts to appear to be quasi-stationary. That is, the problem reduces to determining the instantaneous frequency shift of a higher mode oscillating with a constant amplitude superimposed on top of a slowly modulated base-sample separation $d_1(t)$. This means that first mode vibrations no longer interfere with the frequency shift of the higher mode vibrations induced by nonlinear interaction, therefore, in a sense, vibration modes are *decoupled*.

In Eq. 4.6, the frequency shift Δf_2 is calculated by projecting the force acting on the tip on the higher mode vibrations. Through integration by-parts where we take $dv = \cos\theta\, d\theta$ and $u = F_{ts}(d_1(t)+A_2\cos\theta)$ a simpler, yet powerful expression of the frequency shift is available:

$$\begin{aligned}\Delta f_2(t) &\approx -\frac{\bar{f}_2}{2\pi k_2}\int_{-\pi}^{\pi} F'_{ts}(d_1(t)+A_2\cos\theta)\sin^2\theta\, d\theta = \\ &= -\frac{\bar{f}_2}{4\pi k_2}\left(\int_{-\pi}^{\pi} F'_{ts}(d_1(t)+A_2\cos\theta)d\theta\right. \\ &\quad \left. -\int_{-\pi}^{\pi} F'_{ts}(d_1(t)+A_2\cos\theta)\cos 2\theta\, d\theta\right) \end{aligned} \tag{4.10}$$

We expand $F'_{ts}(\cdot)$ into powers of $A_2\cos\theta$ to simplify Eq. 4.10 and write:

$$\begin{aligned}F'_{ts}(d_1(t)+A_2\cos\theta) &= F'_{ts}(d_1(t)) + F''_{ts}(d_1(t))\ A_2\cos\theta \\ &\quad + \tfrac{F'''_{ts}(d_1(t))}{2}\ A_2^2\cos^2\theta + ...\end{aligned} \tag{4.11}$$

The third and higher order terms in the above expansion are negligible, if the following is satisfied:

$$A_2 \ll 2\left|\frac{F''_{ts}(d_1(t))}{F'''_{ts}(d_1(t))}\right| \tag{4.12}$$

Substituting Eq. 4.11 in Eq. 4.10, the second integral vanishes and we get a simpler result:

$$\Delta f_2(t) \approx -\frac{\bar{f}_2}{4\pi k_2}\int_{-\pi}^{\pi} F'_{ts}(d_1(t)+A_2\cos\theta)\, d\theta \tag{4.13}$$

with the necessary condition of

$$\pi^2 A_1 \frac{\bar{f}_1^{\,2}}{\bar{f}_2} T_c \ll A_2 \ll 2\left|\frac{F''_{ts}(d_1(t))}{F'''_{ts}(d_1(t))}\right| \tag{4.14}$$

Within this range of A_2, the frequency shift is accurately described by the integral in Eq. 4.13. So, the higher mode vibrations "samples" the gradient of the tip-sample force interaction and allows us to quantify $F_{ts}(d)$ in a single cycle of the first mode vibrations T_1, while Δf_1 itself remains sensitive to topographical features.

4.2 Recovery of the force gradient

Eq. 4.13 describes the frequency shift in terms of the force gradient. Solving the inverse problem, i.e., finding the force gradient from the measured frequency shift is more important. In this section, we examine Eq. 4.13 for small A_2 and derive an even simpler expression relating the force gradient to the measured frequency shift.

If A_2 is sufficiently small, while still satisfying the left hand side of Eq. 4.14, we can approximate $A_2 \cos\theta$ with a square wave of same peak values and integral in Eq. 4.13 can be simplified to give:

$$\begin{aligned} \Delta f_2(t) &\approx -\frac{\bar{f}_2}{4k_2}[F'_{ts}(d_1(t)+A_2) + F'_{ts}(d_1(t)-A_2)] = \\ &= -\frac{\bar{f}_2}{2k_2}\overline{F'_{ts}(d_1(t))} \end{aligned} \tag{4.15}$$

Hence, the frequency shift is proportional to the sum of two force gradient functions shifted by $2A_2$ with respect to each other. If A_2 is very small, we can assume:

$$F'_{ts}(d_1(t)) \approx \overline{F'_{ts}(d_1(t))} = -\frac{2k_2}{\bar{f}_2}\Delta f_2(t) \tag{4.16}$$

In this case, Eq. 4.16 can be used directly for recovery. But, because of the condition in Eq. 4.14, A_2 can not be very small. It is possible to recover F'_{ts} from $\overline{F'_{ts}}$ by noting that:

$$F'_{ts}(d-A_2) = 2\overline{F'_{ts}(d)} - F'_{ts}(d+A_2) \tag{4.17}$$

$$F'_{ts}(d) \;\rightarrow\; 0 \quad \text{for } d \rightarrow \infty \tag{4.18}$$

For this purpose, first an interpolation is necessary to get equally spaced samples in d from equally spaced samples in t. The first recovery algorithm can be written as:

1. From the measured $\Delta f_2(t)$ for $t_i = t_{i-1} + \Delta t$, determine $\overline{F'_{ts}(d(t_i))}$ using Eq. 4.15.

2. Interpolate $\overline{F'_{ts}(d(t_i))}$ to get $\overline{F'_{ts}(d_{(j)})}$ with $d_{(j+1)} = d_{(j)} - A_2/m$ where m is an integer chosen to give a sufficient sampling distance in d. j is the sample index. $d_{(0)}$ is chosen sufficiently large so that $F'_{ts}(d_{(0)}) = 0$.

3. Use $F'_{ts}(d_{(j+m)}) = 2\overline{F'_{ts}(d_{(j)})} - F'_{ts}(d_{(j-m)})$ for j=0, 1, 2, ... to recover F'_{ts} function at equally spaced intervals. For initialization we choose $F'_{ts}(d_{(j)}) = 0$ for $j < 0$.

Since this algorithm is sufficiently simple, it can be implemented in real time while the data points are being captured. If the noise between the samples are uncorrelated, the recovery algorithm degrades the signal-to-noise ratio by about $10 \log 5 = 7$ dB. This is a significant loss in signal quality.

One can obtain a better performance in recovery using a more computationally intensive and hence possibly an off-line method. The second algorithm: Assume a model for $F_{ts}(d)$ and find the parameters of the model to satisfy Eq. 4.13 in the least square sense using an optimization method. A possible model is given by Eq. 2.8.

Recovery of the force gradient from $\Delta f_2(t)$ also depends on the available bandwidth of the detection electronics. Suppose that the bandwidth is not large enough to capture the fast changes of $\Delta f_2(t)$ and an aggregate effect is observed. For example, a reception bandwidth smaller than $\bar{f}_1$ means an averaging

of Eq. 4.13 along T_1, and we get an averaged frequency shift, $\langle \Delta f_2 \rangle$, of the higher mode vibrations:

$$\langle \Delta f_2 \rangle \approx -\frac{\bar{f}_2}{4\pi k_2} \int_{-\pi}^{\pi} F'_{ts}(Z_0 + A_1 \cos\phi)\, d\phi, \tag{4.19}$$

which is the expression published recently by Kawai *et al.* to describe the observed frequency shift of the higher mode vibrations in bimodal dynamic force microscopy [32]. Notice that in this case, $\langle \Delta f_2 \rangle$ is sensitive to large features of $F_{ts}(d)$ and the technique is similar to bimodal AM-AFM where phase shifts are constant during the slow oscillation.

4.3 Sensitivity

The ambiguity in the frequency measurement of the higher mode vibrations is given by [19, 37]:

$$\delta f_2 = \sqrt{\frac{\bar{f}_2 k_B T B}{\pi k_2 Q_2 A_2^2} + \frac{N_d^2 B^3}{6A_2^2}} \tag{4.20}$$

where k_B is the Boltzmann constant, T is the absolute temperature, N_d is the detection noise voltage density, B is the detection bandwidth. The detection bandwidth has to be larger than $2/T_c$ in order to capture the harmonic content of the $\Delta f_2(t)$. Assuming that $T_c \approx T_1/10$ we take $B = 20\bar{f}_1$. In such a case, the ambiguity in the reconstruction of the force gradient from the frequency shift data can be calculated by noting that $F'_{ts}(t) = -2(k_2/\bar{f}_2)\Delta f_2(t)$, therefore multiplying Eq. 4.20 by $2k_2/\bar{f}_2$ to get:

$$\delta F'_{ts} \approx \sqrt{\frac{80 k_B T \bar{f}_1}{\pi Q_2 A_2^2 \bar{f}_2} k_2 + 5 \cdot 10^3 \frac{N_d^2 \bar{f}_1{}^3}{A_2^2 \bar{f}_2{}^2} k_2^2}. \tag{4.21}$$

Assuming that the amplitude of the higher mode vibrations is $A_2 = 0.2$ nm, $f_1 = 50$ kHz for high scan speeds, $\bar{f}_2/\bar{f}_1 \approx 100$ to acquire repulsive forces, $Q_2 = 10000$ which is typical in vacuum, $N_d = 10$ fm/$\sqrt{\text{Hz}}$ [38], and at room temperature we have $\delta F'_{ts} \approx 1$ N/m if $k_2 \approx 100$ N/m. The relation $k_2 = k_1(\bar{f}_2/\bar{f}_1)^2$ holds to a

good extend for rectangular cantilevers therefore $k_1 \approx 10$ mN/m which is small. This reveals that rapid imaging and at the same time achieving low frequency noise levels might be possible by using long, narrow and thin cantilevers for which the ratio $\bar{f}_1/k_1$ (which determines the sensitivity to topographical variation) is high for small k_1.

4.4 Modeling and simulations

Our theoretical conclusions are based on numerous assumptions such as the tip motion being purely bi-harmonic therefore Δf_1 and Δf_2 being small compared to $\bar{f}_1$ and $\bar{f}_2$, respectively [3], $\bar{f}_2$ being much greater than $\bar{f}_1$, and finally A_2 being small enough. Instead of analyzing the restrictions of such a complicated list of assumptions, we go on with testing our predictions Eq. 4.13, Eq. 4.15 and Eq. 4.16 by doing realistic simulations of the AFM dynamics.

In our simulations vibration modes are represented by two coupled point like spring-mass systems. Let us write down the equation of motion (see Eq. 2.2):

$$m_i \frac{d^2 z_i}{dt^2} + \gamma_i \frac{dz_i}{dt} + k_i z_i = F_{ext}(t) \tag{4.22}$$

where γ is the damping coefficient of the system. We re-write Eq. 4.22 as:

$$L_i \frac{d^2 q_i}{dt^2} + R_i \frac{dq_i}{dt} + \frac{q_i}{C_i} = V(t) \tag{4.23}$$

to recognize that this is the equation for a series RLC circuit and is equivalent to Eq.4.22 if the following assignments are done:

$$L_i = m_i, R_i = \gamma_i = \frac{m_i \omega_i}{Q_i}, C_i = \frac{1}{k_i} \tag{4.24}$$

Appealing to the analogy between Eq. 4.22 and Eq. 4.24, i.e., the analogy between mechanical and electrical state variables, we say that charge is analogous to displacement, and the time derivative of charge, current, is analogous to the

time derivative of displacement, which is velocity. Force is then equivalent to voltage. Suppose that we also have a non-linear device which will provide us with $F(t)$ if supplied with tip sample distance $d(t)$ and other parameters relevant to tip-sample interaction. Then it is possible to simulate the dynamics of the force microscopy to a good approximation, and for an arbitrary set of interaction schemes. That kind of non-linear modeling is available in most of the SPICE based circuit simulators. We used Advanced Design System (ADS) for simulations.

The vibration modes are coupled through a nonlinear component output of which is described by [36]:

$$F_{ts}(d) = \begin{cases} -F_{max}/(1+30(d-a_0)^2) & \text{for } d \geq a_0 \\ -F_{max} + S_{rep}(d-a_0)^2 & \text{for } d < a_0, \end{cases} \tag{4.25}$$

where F_{max} represents the maximum of the attractive forces, S_{rep} is the strength of the repulsive interaction and a_0 is the interatomic distance separating attractive and repulsive force regimes. All forces are in nN, all distances are in nm and S_{rep} has units of nN nm^{-2}. Since the derivative of F_{ts} with respect to tip sample distance is continuous regardless of the contact parameters if the interaction is given by Eq. 4.25, it is preferred over the DMT model (see Eq. 2.8) of the tip sample forces. See Fig. 4.4 for a comparison of forces in our model and the DMT model.

For all simulations $\bar{f}_1 = 100$ kHz, first mode stiffness $k_1 = 10$ N/m, $Q_1 = 200$ and $Q_2 = 1000$. Resonant frequency of the higher mode ($\bar{f}_2$) is either 3 MHz or 10 MHz. Stiffness of the higher mode is given by $k_2 = k_1(\bar{f}_2/\bar{f}_1)^2$. $\bar{f}_2 = 3 - 10$ MHz. Fixed time stepping and Gear's method for integration with maximum Gear order set to 5 is used. Using other methods of time step control, namely iteration count or truncated error, causes convergence problems and cannot accurately represent the place of the second resonance. Time step is fixed at $1/f_1/2^{15}$.

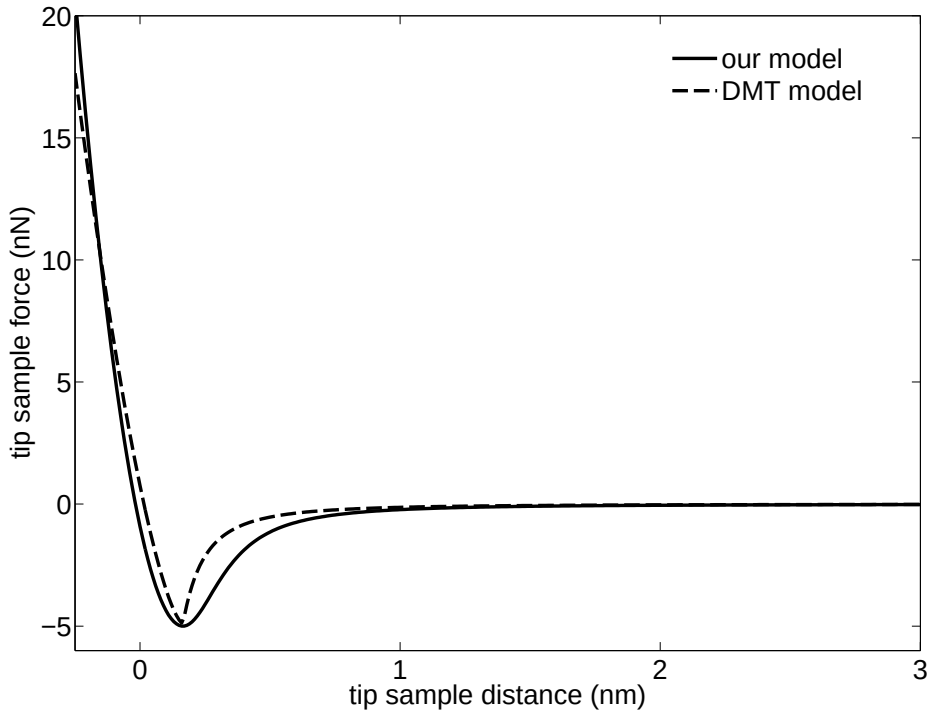

Figure 4.4: Tip sample forces with respect to tip sample distance. Dashed line is given by the DMT model for which $E = 20$ GPa, $R = 10$ nm, $H = 8 \cdot 10^{-20}$. Solid line is given by Eq. 4.25 such that $F_{max} = 5$ nN, $S_{rep} = 150$ nN. Note that in DMT model the transition from attractive to repulsive forces is abrubt, while this transition occurs smoothly in our model.

In order to simulate bimodal FM-AFM, two positive feedback loops are needed to maintain 90° of phase shift between the vibrations of the tip and the actuation and to keep A_1 and A_2 constant. This is similar to single mode FM-AFM but now with an additional vibration channel. On the positive feedback, transmission lines are used to fine tune the phase introduced at the desired frequency. Positive feedback assures that poles of the system are on the imaginary line such that once excited cantilever vibrates with a constant amplitude, however, automatic gain circuitries are needed to compensate for the lost energy. To do this A_1 and A_2 has to be determined. A synchronous detector wouldn't work because oscillation frequencies are not constant. Our solution is to square

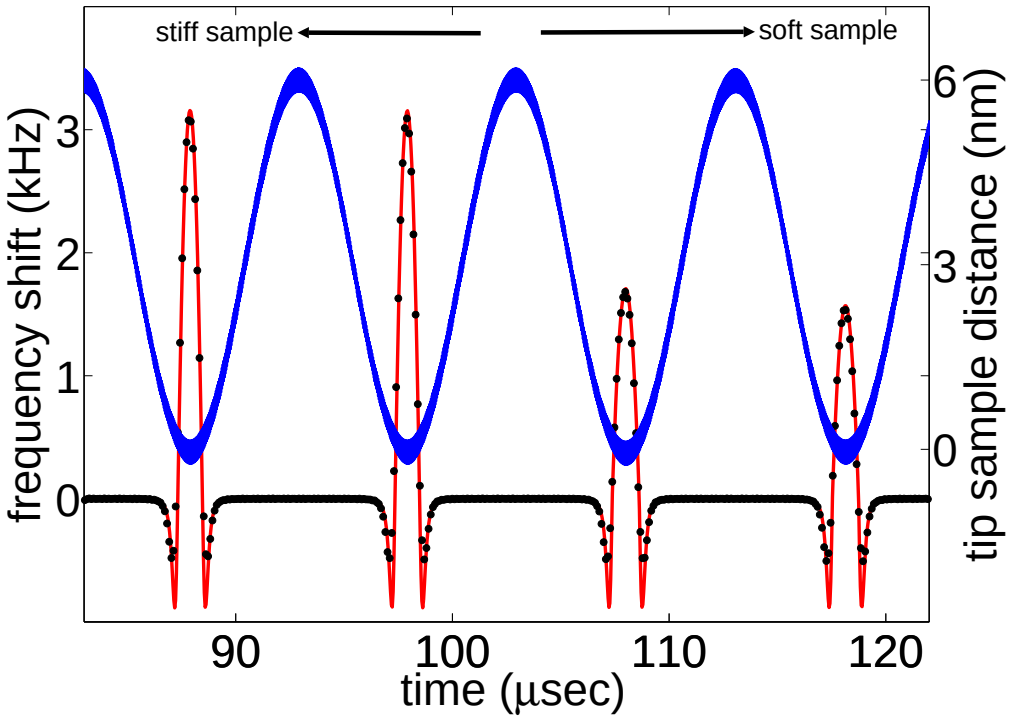

Figure 4.5: Instantaneous frequency shift of the higher mode and tip sample distance with respect to time. Frequency shift is calculated using Eq. 4.16 and dots are obtained from the simulation. $A_1 = 3$ nm, $A_2 = 0.2$ nm, $Z_0 = 3$ nm, $f_2 = 10$ MHz. $F_{max} = 5$ nN, $S_{rep} = 150$ nN nm^{-2} until 100 μs and $S_{rep} = 75$ nN nm^{-2} after 100 μs.

the displacement signal, low-pass filtering it and filtering out the harmonics, subtracting from a reference after taking the square root and use the result as the error signal. Proportional integral controllers use error signals to extract desired control signals. Control signals then determine the gains of the positive feedback loops. In order to determine $\Delta f_2(t)$, $d(t)$ is recorded and zero crossings of the higher mode vibration are used to calculate frequency shifts. For schematic description of the technique see Fig. 4.1.

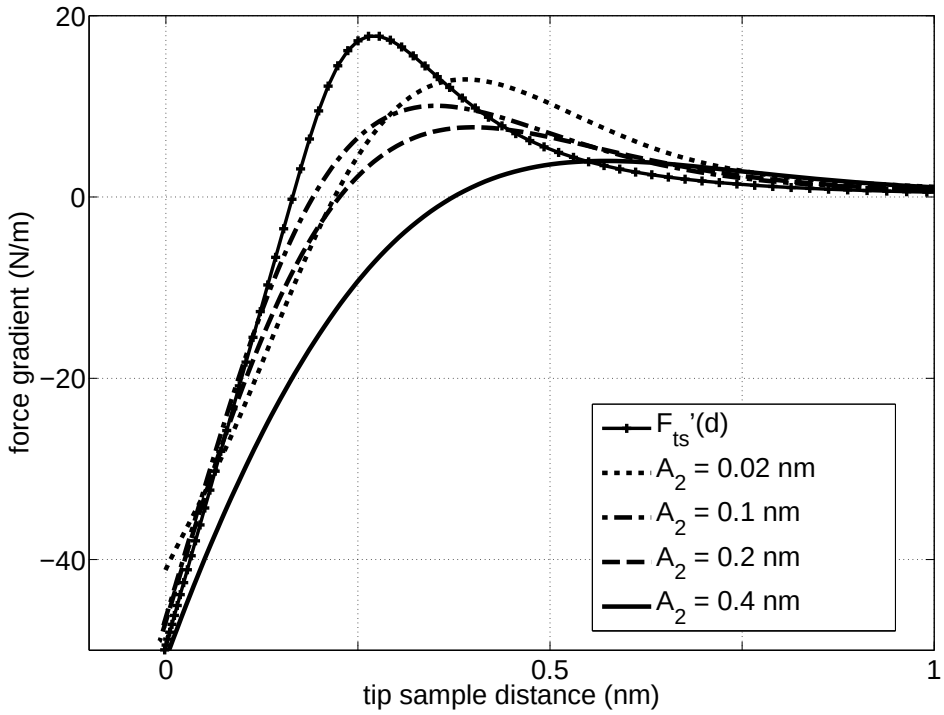

Figure 4.6: Actual force gradient $F'_{ts}(d)$ and force gradient curves obtained from frequency shift data with respect to tip sample distance. $A_1 = 10$ nm, $Z_0 = 10$ nm, $\bar{f}_2 = 10$ MHz, $F_{max} = 5$ nN, $S_{rep} = 150$ nN nm^{-2}.

4.5 Results and discussions

Fig. 4.5 shows the simulation results for the instantaneous frequency shift of the higher mode as a function of time. The sample is assumed to be perfectly flat, but it has two regions with different force curves. As seen in the figure, the frequency shifts are largest when the tip is nearest to the sample. The scan speed is limited by the period of low frequency drive. As expected, the sensitivity of the higher mode vibrations to surface property variations are instantaneous, therefore independent of the quality factor of the higher mode.

The force gradient can be calculated from the frequency shift data, assuming that Eq. 4.16 is sufficient to describe the dynamics. Fig. 4.6 shows such a calculation along with the actual curve for $F'_{ts}(d)$. The accuracy of the reconstruction

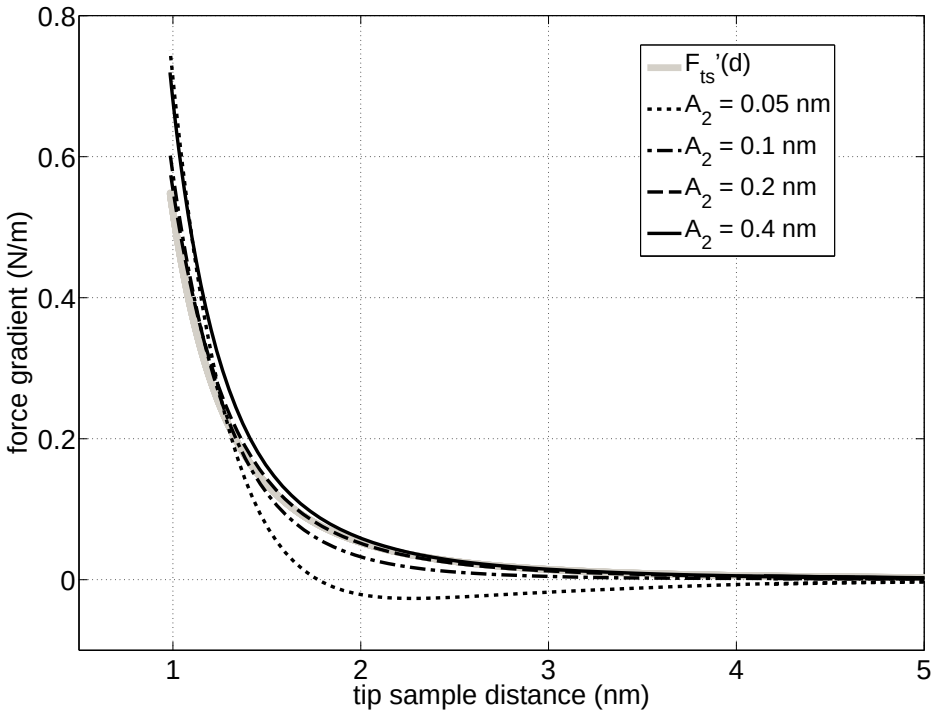

Figure 4.7: Actual force gradient $F'_{ts}(d)$ (in gray) and force gradient curves obtained from frequency shift data with respect to tip sample distance. $A_1 = 3$ nm, $Z_0 = 4$ nm, $\bar{f}_2 = 3$ MHz, $F_{max} = 5$ nN, $S_{rep} = 150$ nN nm^{-2}.

of the force gradient degrades as the vibration amplitude of the higher mode increases. This is the case, since larger vibration amplitudes imply a non-zero contribution of the last term in Eq. 4.10, therefore the violation of condition in Eq. 4.12. On the other extreme, that is when $A_2 < 0.1$ nm, reconstruction begins to deteriorate. This is the point beyond which $A_1 f_1 > A_2 f_2$, such that vibration modalities are no longer decoupled. The effect is more pronounced in Fig. 4.7 where $\bar{f}_2 = 3$ MHz, and base sample separation $Z_0 = 4$ nm. Reconstruction is almost perfect for $A_2 = 0.2$ nm for which $A_1 f_1 \ll A_2 f_2$ holds. However, for $A_2 = 0.1 - 0.05$ nm quasi-stationarity is not satisfied, hence the distortion in the gradient reconstruction. Note that in Fig. 4.6 gradient of the repulsive forces are accurately represented for almost all values of the higher mode vibration amplitude. This is because repulsive regime corresponds to the the lower

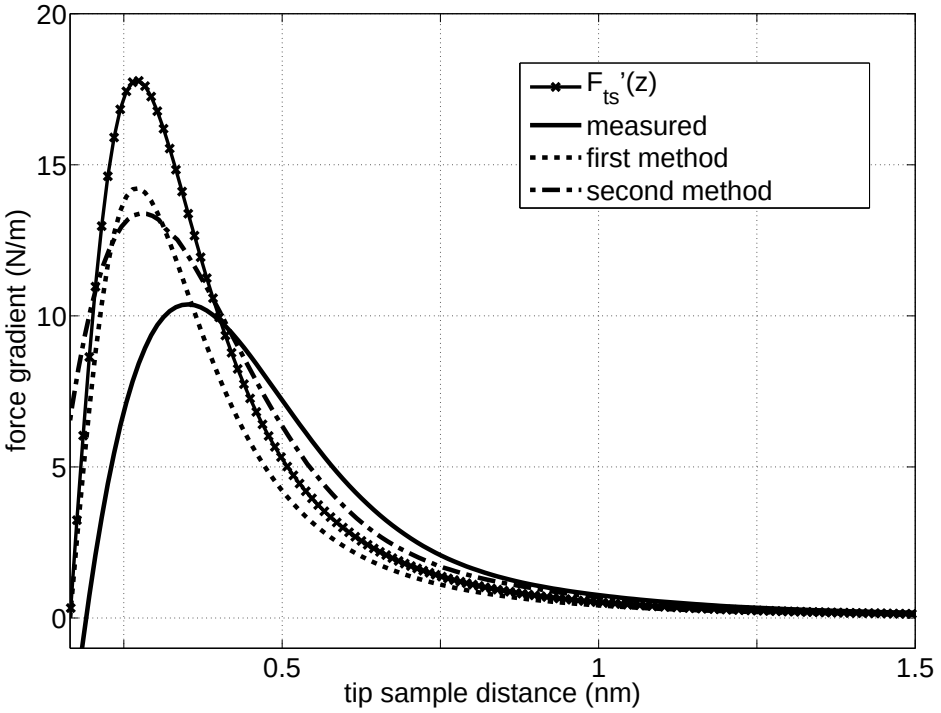

Figure 4.8: Actual force gradient $F'_{ts}(d)$ and force gradient estimate obtained from Eq. 4.16 along with the force gradient curves reconstructed using the first recovery algorithm and the second algorithm. $A_1 = 10$ nm, $A_2 = 0.1$ nm, $Z_0 = 10$ nm, $\bar{f}_2 = 10$ MHz, $F_{max} = 5$ nN, $S_{rep} = 150$ nN nm^{-2}.

turning point of $d_1(t)$ for which Eq. 4.14 is best satisfied. The opposite is true for the reconstruction of the gradient of the attractive forces. Therefore for the attractive regime, i.e., for the positive values of the force gradient, it might be necessary to use correction algorithms.

Fig. 4.8 shows the results of the recovery algorithms in comparison to uncorrected data. The recovered force gradients are not perfect, but they are definitely better than the uncorrected version. Hence it is worthwhile to use one of the recovery algorithms for better accuracy.

Let us now discuss the possible ways of achieving larger frequency shifts in bimodal FM-AFM. Referring to Eq. 4.13 it is clear that the resonance frequency of the higher mode has to be chosen large for this purpose. Large $\bar{f}_2$ also allows

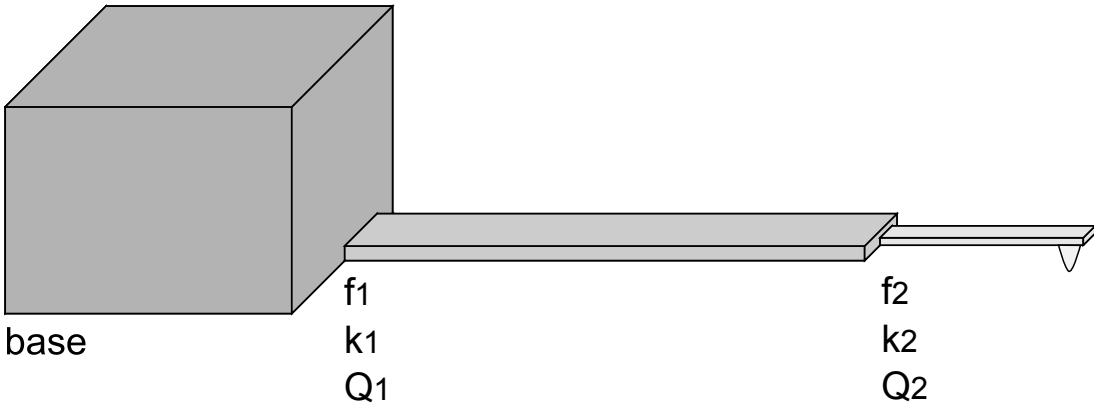

Figure 4.9: Schematic description two cantilevers connected end to end. Large cantilever with resonance frequency $\bar{f}_1$ provides slow oscillations and small cantilever with resonance frequency $\bar{f}_2$ provides fast oscillations to extract the force gradient.

us to chose small vibration amplitude A_2 and to satisfy the condition in Eq. 4.14 such that tip sample forces with sharp nonlinearities can be recovered. However, eigenmodes with large $\bar{f}_2$ typically implies large spring constant k_2 for a rectangular cantilever. Therefore for better performance it is essential to design cantilevers with a mode having high resonance frequency to stiffness ratio. See pg. 24 for a discussion. Fabricating a mechanical sensor where two cantilevers are connected end to end might be one solution to this problem; i.e., a large cantilever clamped to the substrate will provide slow oscillations in the low kHz region and a much smaller beam in series to the first will oscillate in the MHz region and will extract the tip sample force gradient. See Fig. 4.9. Another possibility is to use the torsional mode, which is preferred in harmonic imaging for its high resonance frequency to stiffness ratio. However exploiting the torsional motion of a beam in bimodal FM-AFM requires a "torsional excitation" at the base.

Notice that bandwidth of the signal $\Delta f_2(t)$ is on the order of $10\bar{f}_1$, therefore bimodal FM-AFM requires high performance frequency demodulators with bandwidths reaching up to 1 MHz. Recent development of low-noise, wide bandwidth

frequency demodulators ($\sim$ 100 kHz) [39] indicates that it is possible to simultaneously achieve high imaging rates and compositional contrast by a careful application of bimodal FM-AFM.

Finally, we note that bimodal FM-AFM is a strong candidate for force spectroscopy especially in vacuum environment where the large quality factor of the vibration mode limits the imaging bandwidth of amplitude modulation techniques, namely harmonic imaging and bimodal AM-AFM.

Chapter 5

IMPLICATIONS TO BIMODAL AM-AFM

Observed phase contrast in bimodal AM-AFM can be explained using the concept of spring softening instead of virials and energy conservation. The problem boils down to determining the "average force gradient" $\langle k_{ts} \rangle$ experienced by the higher order vibrations during the period of the slow oscillation $T_1 = 1/f_1$. The resonance shift caused by the average force gradient can then be used to calculate the phase shift ϕ_2.

The phase of the higher mode shifts along with the resonance frequency. If we assume that the excitation frequency coincides with the natural resonance frequency f_2, the phase shift ϕ_2 can be calculated using Eq. 2.9 and Eq. 2.12:

$$\phi_2 = \frac{\pi}{2} + \arctan\left(\frac{Q_2\langle k_{ts}\rangle/k_2}{\sqrt{1-\langle k_{ts}\rangle/k_2}}\right) \tag{5.1}$$

Notice that ϕ_2 is not a function of time. This is the case since the phase shifts are not instantaneous like the frequency shifts in FM-AFM. Note that the phase difference between the oscillation and drive is $\pi/2$, if there is no tip sample interaction, i.e., when $\langle k_{ts} \rangle = 0$.

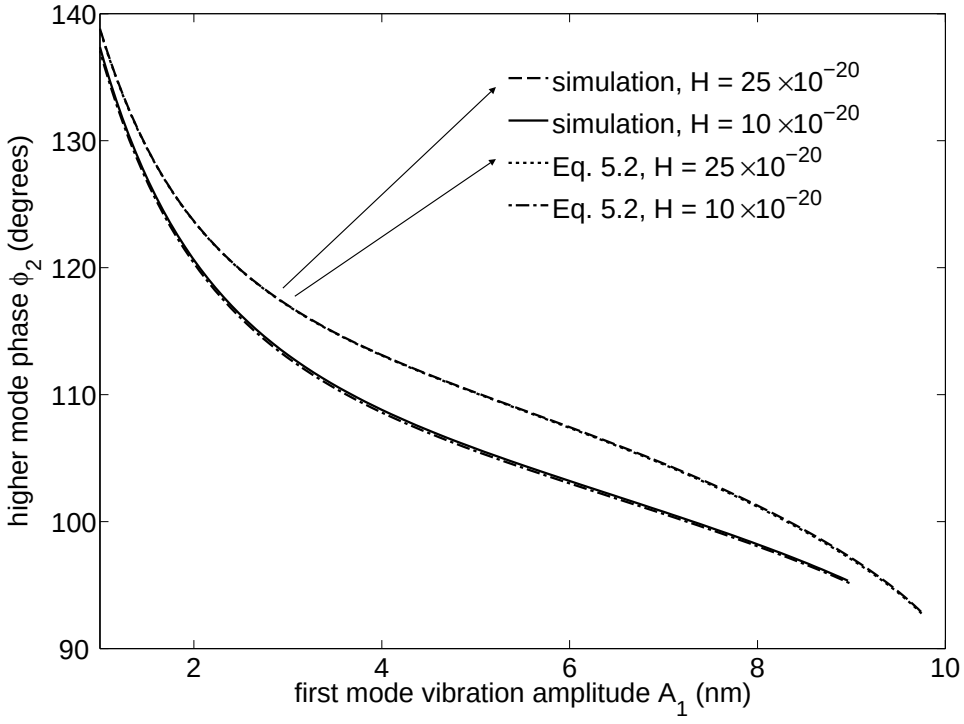

Figure 5.1: The phase shift ϕ_2 as a function of the first mode amplitude A_1. $H = 25 \cdot 10^{-20}$ for the higher curve, $H = 10 \cdot 10^{-20}$ for the lower curve. $A_2 = 0.5$ for simulations.

Eq. 4.19 describes higher mode frequency shifts in FM-AFM due to tip-sample force gradient under the condition that detection electronics is not sensitive to fast variations. The same equation can be used to define the average force gradient $\langle k_{ts} \rangle$ experienced by higher order vibrations by noting that $\langle \Delta f_2 \rangle = -\bar{f}_2 \langle k_{ts} \rangle / 2k_2$ (see Eq. 2.13), therefore:

$$\langle k_{ts} \rangle = \frac{1}{T_1} \int_0^{T_1} F'_{ts}(Z_0 + A_1 \cos(2\pi f_1 \tau))\, d\tau \tag{5.2}$$

Eq. 5.2 along with Eq. 5.1 and Eq. 2.22 (which gives the relation between A_1 and Z_0) describes the phase shifts observed in bimodal AM-AFM in a rather intuitive and simple way. Note that in writing down Eq. 5.2 we assumed that $A_{20} \ll A_{10}$, i.e., the higher mode vibration amplitude is negligible. Therefore, using Eq. 5.2 we cannot quantify the effect of the higher mode vibration amplitude A_{20} on phase contrast.

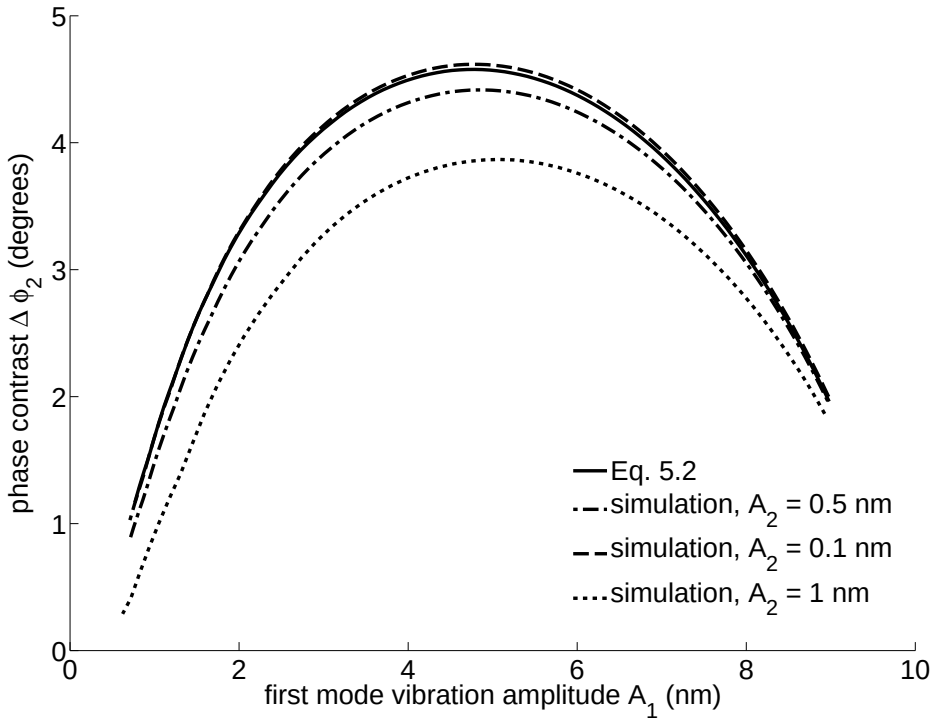

Figure 5.2: Phase contrast $\Delta\phi_2$ with respect to first mode amplitude A_1. Contrast is obtained from Fig. 5.1 by subtracting phase shifts belonging to different H. Solid line is the prediction Eq. 5.2. Dashed lines are from simulations.

We compare analytical results with realistic simulations of bimodal AM-AFM. We take $f_1 = 50$ kHz, $f_2 = 310$ kHz, $k_1 = 0.5$ N/m, $k_2 = 20$ N/m, $Q_1 = 250$, $Q_2 = 1000$, $A_{10} = 10$ nm, $A_{20} = 0.1 - 1$ nm, use DMT model for the tip sample forces where $E = 200$ MPa, $R = 20$ nm, $a_0 = 0.165$ nm, $H = 10 - 25 \cdot 10^{-20}$. In Fig. 5.1 phase shift ϕ_2 is plotted with respect to first mode vibration amplitude A_1. The phase shift predicted using Eq. 5.2 shows excellent agreement with simulations. Fig. 5.2 shows phase contrast between two samples for which Hamaker constants are different. Again, the phase contrast achieved in bimodal AM-AFM is successfully explained by our analytic approach. Notice that the maximum phase contrast is attained at a specific A_1. Let us also remind that the phase contrast with respect to A_1 is relevant to us since cantilever oscillations settle to a fixed oscillation amplitude $A_1 = A_{set}$ in AM-AFM.

The small initial values of higher mode vibration amplitude A_{20} implies larger phase shifts (this is not apparent from Eq. 5.2, since we assumed that A_{20} is negligibly small). Notice that in Fig. 5.2 the phase contrast increases by 1° as A_{20} decreases from 1nm to 0.1nm. The general trend is that as the vibration amplitude of the second mode decreases, the phase contrast converges to a maximum value. However, small oscillation amplitudes can be buried under the detection noise which degrades the signal to noise ratio. Therefore, the optimum value of A_{20} depends on the density of thermal and detection noise. Note that measuring shifts in ϕ_2 instead of A_2 leads to a better signal to noise ratio. This is not because the phase shifts are more "sensitive" to force gradients, but because the measurement noise on phase is smaller (see Eq. 2.27 and Eq. 2.28). By calculating the rate of change of the phase and amplitude response of the mode (see Eq. 2.9) it is possible to compare sensitivities of the phase and amplitude to gradient variations to see that they are equal.

Determining the optimum value for the free air vibration amplitude of the first mode A_{10} for which the phase contrast is maximized requires deriving closed form expressions for ϕ_2. Finding the exact solution to this problem is hard, since the relation between A_1 and Z_0 is complicated (see Eq. 2.22). However using the asymptotical solution presented in Chapter 2, i.e., Eq. 2.23, we can obtain an approximation which is true for most of the base sample separations for which $Z_0 < A_{10}$. Indeed the region where base sample separation is smaller than the free vibration amplitude is the region of interest. However, doing so does not reveal the mechanisms of phase contrast. The reason is that the solution in Eq. 2.23 assumes a constant difference between Z_0 and A_1 (difference $Z_0 - A_1$ is the minimum of tip sample distance so let us call this parameter d_{min}), i.e., as Z_0 is decreased A_1 decreases linearly. That is not the case. Indeed, if we examine Eq. 5.2 closer, we see that $\langle k_{ts} \rangle$ is maximized when the difference between Z_0

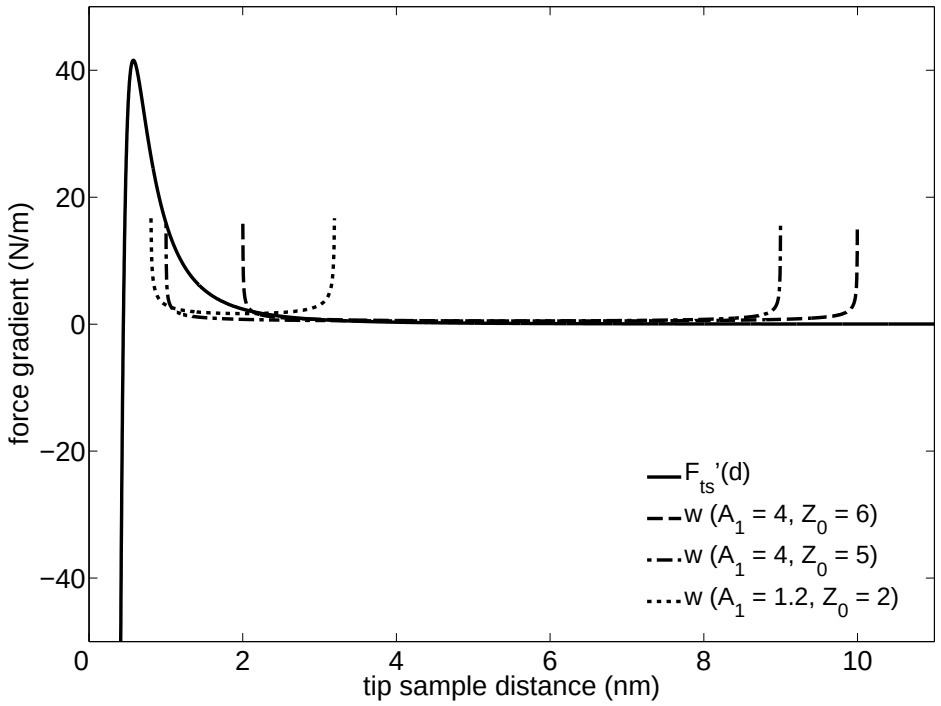

Figure 5.3: Force gradient with respect to tip sample distance along with the weight functions for different base sample separations Z_0 and first mode amplitude A_1

and A_1 is minimized. This means higher contribution from the portions of $F'_{ts}(d)$ where tip is closer to surface and gradient of the tip sample forces are higher.

This is better understood if we make a change of variables $u = A_1 \cos(2\pi f_1 t)$ and transform the integral in Eq. 5.2 into:

$$\langle k_{ts} \rangle = \frac{HR}{3\pi} \int_{-A}^{A} \frac{du}{(Z_0 + u)^3 \sqrt{A^2 - u^2}} \tag{5.3}$$

This is the integration of gradient of the tip sample forces over the tip sample distance, however weighted with a function which is increasingly larger for smaller tip sample separations. Fig. 5.3 shows the gradient of tip sample forces along with different weighting functions for different Z_0 and A_1. In this example d_{min} decreases from 2 nm to 0.8 nm as the base sample separation decreases from 6 nm to 2 nm. Also see Fig. 5.4 for $\langle k_{ts} \rangle$ as a function of vibration amplitude A_1, and

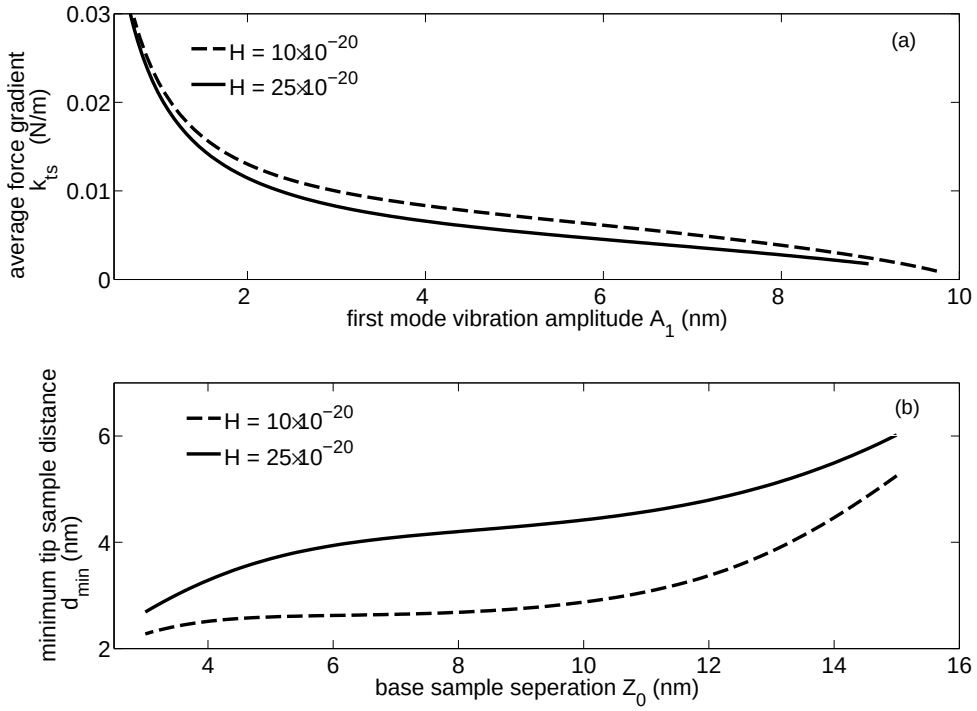

Figure 5.4: (a) Average force gradient with respect to first mode vibration amplitude. (b) Minimum tip sample distance with respect to base sample separation. $H = 10 \cdot 10^{-20}$ for dashed lines, $H = 25 \cdot 10^{-20}$ for solid lines.

d_{min} with respect to base sample separation. Notice that as Z_0 is decreased d_{min} decreases and then the oscillation is squeezed from below by the surface forces. For smaller Z_0 minimum tip sample distance d_{min} decreases rather slowly. On the other hand $\langle k_{ts} \rangle$ increases with decreasing Z_0 and therefore d_{min}. So one could propose that in order to obtain high phase contrast A_{set} should be chosen small such that $\langle k_{ts} \rangle$ is maximized. That would be wrong, since a large $\langle k_{ts} \rangle$ implies larger phase shift ϕ_2 (see Fig. 5.1 together with Fig. 5.4), the phase contrast $\Delta\phi_2$ is not given by Eq. 5.1.

Let us find the rate of change of phase as Hamaker constant changes. But before doing that, we approximate Eq. 5.1 by writing:

$$\phi_2 \approx \pi/2 + \arctan(\frac{Q_2}{k_2}\langle k_{ts} \rangle) \tag{5.4}$$

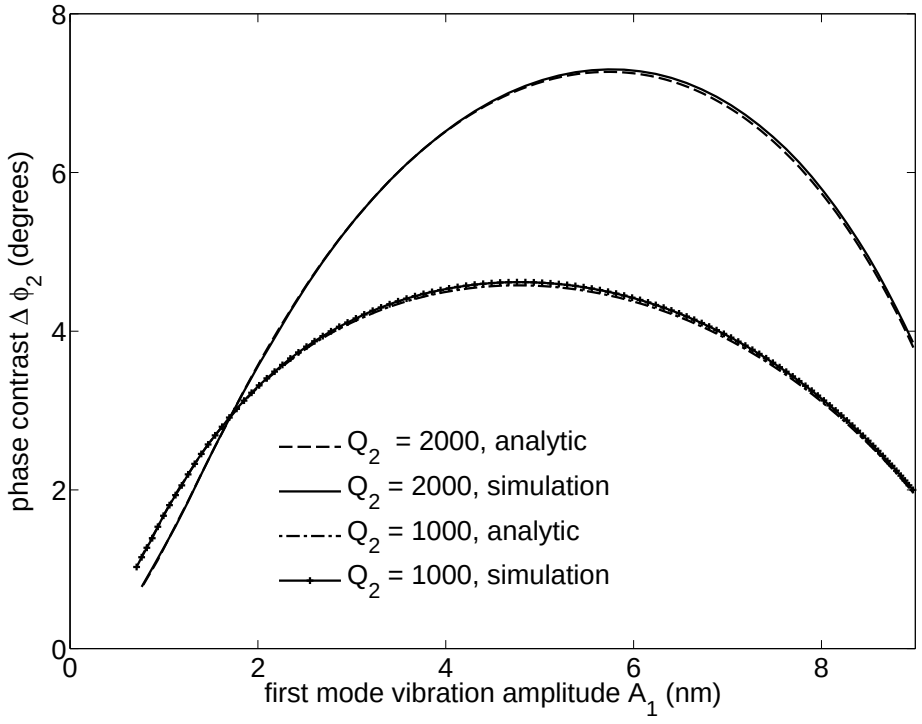

Figure 5.5: Phase contrast for $Q_2 = 1000$ and $Q_2 = 2000$ with respect to first mode vibration amplitude. Dashed lines are obtained from simulations, solid lines are predicted by Eq. 5.2.

This is possible since $\langle k_{ts} \rangle$ is usually much less than 1 N/m. Differentiating Eq. 5.4 with respect to H we get:

$$\frac{\partial \phi_2}{\partial H} = \frac{\frac{Q_2}{k_2}\frac{\langle k_{ts} \rangle}{H}}{1 + \left(\frac{Q_2}{k_2}\langle k_{ts} \rangle\right)^2} \tag{5.5}$$

For the maximum phase contrast we have to maximize the above expression. This can be done over $\langle k_{ts} \rangle$ or over the ratio Q_2/k_2. It depends on the constants of the experiment. For example, if the cantilever parameters are fixed, then Q_2/k_2 is usually known for higher order modes, and one should maximize Eq. 5.5 over $\langle k_{ts} \rangle$ to find best A_{10}. On the other hand, if A_{10} is fixed, then $\langle k_{ts} \rangle$ is known to lie within a region, and the maximization has to be done over Q_2/k_2 to chose the optimum value of quality factor and stiffness. Since Eq. 5.5 is symmetric with respect to interchanging Q_2/k_2 and $\langle k_{ts} \rangle$ the result would not change. So,

differentiating Eq. 5.5 with respect to Q_2/k_2 or $\langle k_{ts} \rangle$ and equating the result to zero we get a surprisingly simple relation:

$$\frac{Q_2}{k_2} = \frac{1}{\langle k_{ts} \rangle} \tag{5.6}$$

Now let us reiterate. Assume somehow that one is restricted with choosing only some values of A_{10}. Indeed this is the case in practice. For large A_{10}, repulsive solutions are realized. This is undesirable, since it defeats the purpose of imaging using gentle forces. Further, if repulsive forces can be tolerated, the phase shifts of the first mode vibrations due to energy dissipation should be considered for obtaining compositional contrast. On the other hand, for small A_{10} establishing the feedback loop becomes problematic. Therefore, since A_{10} is known to lie within a region, then $\langle k_{ts} \rangle$ is also known to lie within a region. As an example, for $A_{10} = 10$ nm, Fig. 5.4 shows that $\langle k_{ts} \rangle$ lies within the narrow band of 4-6 mN/m for reasonable values of A_1, i.e., for $5 \leq A_1 \leq 8$. Using Eq. 5.6, now we can now easily find the optimum Q_2/k_2 to reach maximum phase contrast for $5 \leq A_1 \leq 8$ and design the geometry of the cantilever accordingly.

For the problem at hand, i.e., for the experimental conditions described at pg. 56, the phase contrast within the region $5 \leq A_1 \leq 8$ can be improved by choosing $Q_2/k_2 = 1/0.005 = 200$ m/N and in such a case Q_2 has to be changed from 1000 to 2000. In Fig. 5.5 we see that by doing so, the phase contrast improves by a factor of almost two and is maximized within the region $5 \leq A_1 \leq 8$ as it was intended.

We remark that further properties bimodal AM-AFM might be left unstudied here due to lack of time and space. However we are confident that understanding and mathematical tools presented in this chapter is powerful enough to discover and explain them in detail.

Chapter 6

CONCLUSIONS

Atomic force microscopy has evolved from the very simple idea of touching things that we cannot see. However, the application of this requires us to incorporate different fields like contact mechanics, electronics and control theory together. This takes AFM from being just a useful tool to investigate the structures made up of a handful of atoms and molecules, and makes it a theoretically interesting problem to examine, since such a focus on complex properties of AFM induces better understanding of existing techniques and emergence of new ideas in sensor technology.

In this thesis we have adopted the use of bimodal excitation of the cantilever in AFM using amplitude modulation and applied it to its frequency modulation counterpart. We have shown from first principles that the technique is the dual of harmonic imaging using torsional cantilevers, i.e., using bimodal FM-AFM we can acquire surface forces by employing the sensitivity of an higher mode to changes in the interaction of the sinusoidal motion of the tip with the non-linear tip-sample forces. The difference of bimodal FM-AFM from harmonic imaging is that the scan speed is not limited with the finite quality factor of

the cantilever since in bimodal FM-AFM the lost energy is compensated by an additional feedback loop.

On our way of developing mathematical tools to understand bimodal FM-AFM, we realized that they are also useful to explain the phase contrast mechanism in bimodal AM-AFM. We showed that the problem can be reduced to the solution of a simpler problem in a single mode AM-AFM and sensitivity to compositional features of the sample can be optimized by a proper selection of the ratio Q_2/k_2 of the higher mode. This result will allow researchers to design specific mechanical probes which are optimally sensitive to variations of the surface density.

Future work should consist of doing the actual experiments to confirm these results. One can expect that doing so will lead to new and unforseen problems and questions, and understanding them will give rise to new technologies.

APPENDIX A

Derivation of Eq. 2.14

Let us write down the governing equations of motion of a single mode of a cantilever:

$$m\frac{d^2z}{dt^2} + \frac{m\omega_1}{Q}\frac{dz}{dt} + kz = F_{ext}(t) = F_{ts}(t) + F_0\cos(\omega t) \tag{A.1}$$

The term $\frac{m\omega_1}{Q}\frac{dz}{dt}$ represents dissipative forces. Dissipative forces are responsible for the exponential decay of the oscillation amplitude. In FM-AFM dissipative forces are compensated by the drive $F_d = F_0\cos(\omega t)$ so that oscillation amplitude A does not decay and stays constant, i.e. $F_0\cos(\omega t) = \frac{m\omega_1}{Q}\frac{dz}{dt}$. This reduces Eq. A.1 into:

$$m\frac{d^2z}{dt^2} + kz = F_{ts}(t) \tag{A.2}$$

Due to harmonic approximation we take that tip motion is sinusoidal, $z = A\cos(\omega t)$. Plugging z into Eq. A.2 we get:

$$-m\omega^2 A\cos(\omega t) + kA\cos(\omega t) = F_{ts}(t) \tag{A.3}$$

Multiplying both sides by $\cos(\omega t)$ and averaging over a single period $1/f_1$ yields:

$$-\frac{m\omega^2}{2}A + \frac{k}{2}A = f_1\int_0^{1/f_1} F_{ts}(t)\cos(\omega_1 t)\,dt \tag{A.4}$$

where we assumed that since frequency shifts are small, $\cos(\omega t)$ in the integral can be approximated by $\cos(\omega_1 t)$. Now recall that $\omega_1 = \sqrt{\frac{k}{m}}$. Plugging $k = m\omega_1^2$ into Eq. A.4 we arrive at:

$$\begin{aligned} f_1 \int_0^{1/f_1} F_{ts}(t)\cos(\omega_1 t)\,dt &= -A\frac{m}{2}(\omega^2 - \omega_1^2) \\ &= -Am\omega_1(\omega - \omega_1) \\ &= -Am4\pi^2 f_1 \Delta f_1 \end{aligned} \tag{A.5}$$

Note that in the last step we assumed $\omega_1 + \omega \approx 2\omega_1$. Finally using the fact that $m = k/\omega_1^2$ and after a little bit of algebra we get:

$$\Delta f_1 = -\frac{f_1^2}{kA}\int_0^{1/f_1} F_{ts}(t) cos(2\pi f_1 t)\,dt \tag{A.6}$$

APPENDIX B

Phase contrast in single mode AM-AFM

Dissipated energy E_{ts} during one cycle of the tip sample interaction is on the order of 100 eV. See Refs. [40]-[41]. Average dissipated energy during one cycle of oscillation is given by $P_{ts} = E_{ts} \cdot f_1$. Further, the relation between phase shifts and dissipated energy is (see Eq. 2.18):

$$\sin\phi \approx \frac{A}{A_0} + \frac{2QP_{ts}}{kAA_0\omega_1} \tag{B.1}$$

Typically in AM-AFM Q is around 100, A_0 is between $50-100$ nm, stiffness k is in the range $1-10$ N/m and for the dissipation to actually take place oscillation amplitude A is set to %50 of free vibration amplitude A_0 such that repulsive solutions can be realized. Also notice that resonance frequency f_1 appears both in the denominator and the numerator of Eq. B.1. Therefore Eq. B.1 can be simplified to yield:

$$\sin\phi \approx 0.5 + \frac{2QE_{ts}}{kA_0^2\pi} \tag{B.2}$$

and hence:

$$\phi = \arcsin(0.5 + \frac{2QE_{ts}}{kA_0^2\pi}) \tag{B.3}$$

Expanding Eq. B.3 around $E_{ts} = 0$ we get:

$$\phi \approx 0.5 + \frac{2QE_{ts}}{kA_0^2\pi} \tag{B.4}$$

We can now define phase contrast $\Delta\phi$ as:

$$\Delta\phi = \frac{2Q\Delta E_{ts}}{kA_0^2\pi} \tag{B.5}$$

Consider two samples and due to differences in chemical composition dissipated energy E_{ts} differs by 20 eV for the two. By recording the phase of the vibrations in single mode AM-AFM we can distinguish these two samples. In the light of Eq. B.5 and for conditions typical to AM-AFM, 20 eV produces a phase contrast in the range of $0.1 - 5^\circ$ depending on the actual value of the stiffness k and free vibration amplitude A_0.

Bibliography

[1] G. Binnig, C. Quate, and C. Gerber, "Atomic force microscope," *Physical Review Letters*, vol. 56, no. 9, pp. 930–933, 1986.

[2] H. Holscher, W. Allers, U. Schwarz, A. Schwarz, and R. Wiesendanger, "Determination of tip-sample interaction potentials by dynamic force spectroscopy," *Physical Review Letters*, vol. 83, no. 23, pp. 4780–4783, 1999.

[3] F. Giessibl, "A direct method to calculate tip-sample forces from frequency shifts in frequency-modulation atomic force microscopy," *Applied Physics Letters*, vol. 78, no. 1, pp. 123–125, 2001.

[4] F. Giessibl, "Advances in atomic force microscopy," *Reviews of Modern Physics*, vol. 75, no. 3, pp. 949–983, 2003.

[5] O. Sahin, C. Quate, O. Solgaard, and A. Atalar, "Resonant harmonic response in tapping-mode atomic force microscopy," *Physical Review B*, vol. 69, no. 16, p. 165416, 2004.

[6] O. Sahin, S. Magonov, C. Su, C. F. Quate, and O. Solgaard, "An atomic force microscope tip designed to measure time-varying nanomechanical forces," *Nature Nanotechnology*, vol. 2, no. 8, pp. 507–514, 2007.

[7] N. F. Martinez, S. Patil, J. R. Lozano, and R. Garcia, "Enhanced compositional sensitivity in atomic force microscopy by the excitation of the first

two flexural modes," *Applied Physics Letters*, vol. 89, no. 15, p. 153115, 2006.

[8] S. Patil, N. F. Martinez, J. R. Lozano, and R. Garcia, "Force microscopy imaging of individual protein molecules with sub-pico Newton force sensitivity," *Journal of Molecular Recognition*, vol. 20, no. 6, pp. 516–523, 2007.

[9] J. R. Lozano and R. Garcia, "Theory of phase spectroscopy in bimodal atomic force microscopy," *Physical Review B*, vol. 79, no. 1, p. 014110, 2009.

[10] S. Timoshenko, *History of strength of materials*. McGraw-Hill New York, 1953.

[11] K. Y. Yasumura, T. D. Stowe, E. M. Chow, T. Pfafman, T. W. Kenny, B. C. Stipe, and D. Rugar, "Quality factors in micron- and submicron-thick cantilevers," *Journal of Microelectromechanical Systems*, vol. 9, pp. 117–125, 2000.

[12] O. Sahin and A. Atalar, "Simulation of higher harmonics generation in tapping-mode atomic force microscopy," *Applied Physics Letters*, vol. 79, pp. 4455–4457, 2001.

[13] R. Garcia and R. Perez, "Dynamic atomic force microscopy methods," *Surface Science Reports*, vol. 47, no. 6-8, pp. 197–301, 2002.

[14] J. E. Lennard-Jones, "On the determination of molecular fields," *Proceedings of the Royal Society A*, vol. 106, p. 463, 1924.

[15] N. Jalili and K. Laxminarayana, "A review of atomic force microscopy imaging systems: application to molecular metrology and biological sciences," *Mechatronics*, vol. 14, pp. 907–945, 2004.

[16] B. Cappella and G. Dietler, "Force-distance curves by atomic force microscopy," *Surface Science Reports*, vol. 34, pp. 1–104, 1999.

[17] B. V. Derjaguin, V. M. Muller, and Y. P. Toporov, "Effect of contact deformations on the adhesion of particles," *Journal of Colloid and Interface Science*, vol. 53, p. 314, 1975.

[18] F. J. Giessibl, "Forces and frequency shifts in atomic-resolution dynamic-force microscopy," *Physical Review B*, vol. 56, p. 16010, 1997.

[19] T. Albrecht, P. Grutter, D. Horne, and D. Rugar, "Frequency-modulation detection using high-Q cantilevers for enhanced force microscope sensitivity," *Journal of Applied Physics*, vol. 69, no. 2, pp. 668–673, 1991.

[20] S. Paulo and R. Garcia, "Tip-surface forces, amplitude, and energy dissipation in amplitude-modulation (tapping mode) force microscopy," *Physical Review B*, vol. 64, p. 193411, 2001.

[21] S. Paulo and R. Garcia, "Unifying theory of tapping-mode atomic-force microscopy," *Physical Review B*, vol. 66, p. 41406, 2002.

[22] J. P. Cleveland, B. Anczykowski, A. E. Schmid, and V. B. Elings, "Energy dissipation in tapping-mode atomic force microscopy," *Applied Physics Letters*, vol. 72, p. 2613, 1998.

[23] T. Ikehara, J. Lu, M. Konno, R. Maeda, and T. Mihara, "A high quality-factor silicon cantilever for a low detection-limit resonant mass sensor operated in air," *Journal of Micromechanics and Microengineering*, vol. 17, p. 2491, 2007.

[24] N. A. Burnham and R. J. Colton, "Measuring the nanomechanical properties and surface forces of materials using an atomic force microscope," *Journal of Vacuum Science & Technology A*, vol. 7, p. 2906, 1989.

[25] F. J. Giessibl and M. Tortonese, "Self-oscillating mode for frequency modulation noncontact atomic force microscopy," *Applied Physics Letters*, vol. 70, p. 2529, 1997.

[26] S. R. Manalis, S. C. Minne, A. Atalar, and C. F. Quate, "Interdigital cantilevers for atomic force microscopy," *Applied Physics Letters*, vol. 69, p. 3944, 1996.

[27] J. Kokavecz, O. Marti, P. Heszler, and A. Mechler, "Imaging bandwidth of the tapping mode atomic force microscope probe," *Physical Review B*, vol. 73, no. 15, p. 155403, 2006.

[28] G. Schitter, P. Menold, H. Knapp, F. Allgower, and A. Stemmer, "High performance feedback for fast scanning atomic force microscopes," *Review of Scientific Instruments*, vol. 72, no. 8, pp. 3320–3327, 2001.

[29] S. Manalis, S. Minne, A. Atalar, and C. Quate, "High-speed atomic force microscopy using an integrated actuator and optical lever detection," *Review of Scientific Instruments*, vol. 67, no. 9, pp. 3294–3297, 1996.

[30] M. B. Viani, T. E. Schaffer, G. T. Paloczi, L. I. Pietrasanta, B. L. Smith, J. B. Thompson, M. Richter, M. Rief, H. E. Gaub, K. W. Plaxco, A. N. Cleland, H. G. Hansma, and P. K. Hansma, "Fast imaging and fast force spectroscopy of single biopolymers with a new atomic force microscope designed for small cantilevers," *Review of Scientific Instruments*, vol. 70, p. 4300, 1999.

[31] J. R. Lozano and R. Garcia, "Theory of multifrequency atomic force microscopy," *Physical Review Letters*, vol. 100, no. 7, p. 076102, 2008.

[32] S. Kawai, T. Glatzel, S. Koch, B. Such, A. Baratoff, and E. Meyer, "Systematic Achievement of Improved Atomic-Scale Contrast via Bimodal Dynamic Force Microscopy," *Physical Review Letters*, vol. 103, no. 22, p. 220801, 2009.

[33] H. W. Stark and W. M. Heckl, "Fourier transformed atomic force microscopy: tapping mode atomic force microscopy beyond the hookian approximation," *Surface Science*, vol. 457, p. 219, 2000.

[34] M. Balantekin and A. Atalar, "Enhancing higher harmonics of a tapping cantilever by excitation at a submultiple of its resonance frequency," *Physical Review B*, vol. 71, p. 125416, 2005.

[35] O. Sahin, G. Yaralioglu, R. Growa, S. F. Zappe, A. Atalar, C. Quate, and O. Solgaard, "High-resolution imaging of elastic properties using harmonic cantilevers," *Sensors and Actuators A: Physical*, vol. 114, p. 183, 2004.

[36] G. Chawla and S. D. Solares, "Single-cantilever dual-frequency-modulation atomic force microscopy," *Measurement Science & Technology*, vol. 20, no. 1, p. 015501, 2009.

[37] K. Kobayashi, H. Yamada, and K. Matsushige, "Frequency noise in frequency modulation atomic force microscopy," *Review of Scientific Instruments*, vol. 2009, p. 043708, 80.

[38] T. Fukuma, M. Kimura, K. Kobayashi, K. Matsushige, and H. Yamada, "Development of low noise cantilever deflection sensor for multienvironment frequency-modulation atomic force microscopy," *Review of Scientific Instruments*, vol. 76, p. 053704, 2005.

[39] Y. Mitani, M. Kubo, K.-i. Muramoto, and T. Fukuma, "Wideband digital frequency detector with subtraction-based phase comparator for frequency modulation atomic force microscopy," *Review of Scientific Instruments*, vol. 80, no. 8, p. 083705, 2009.

[40] B. Anczykowski, B. Gotsmann, H. Fuchs, J. P. Cleveland, and V. B. Elings, "How to measure energy dissipation in dynamic mode atomic force microscopy," *Applied Surface Science*, vol. 140, pp. 376–382, 1999.

[41] J. Tamayo and R. Garcia, "Relationship between phase shift and energy dissipation in tapping-mode scanning force microscopy," *Applied Physics Letters*, vol. 73, p. 2926, 1998.